

AN INVESTIGATION INTO LEAD TELLURIDE LEAD SULFIDE  
COMPOSITES AND BISMUTH TIN TELLURIDE ALLOYS FOR  
THERMOELECTRIC APPLICATIONS

A Thesis

Presented in Partial Fulfillment of the Requirements for the Degree:

Masters of Science

in the Graduate School of The Ohio State University

By:

Christopher M. Jaworski

The Ohio State University

December 2008

Master's Examination Committee

Approved By

Dr. Joseph P. Heremans, Advisor

Dr. Yann Guezennec

---

Advisor  
Graduate Program in  
Mechanical Engineering

© Copyright by  
Christopher M. Jaworski  
2008

## ABSTRACT

With the global interest in cutting back dependence on non-renewable energy sources, the field of thermoelectricity has recently seen renewed interest. Additionally, several exciting breakthroughs in both nanoscale and bulk materials have led to increased figure of merit  $zT$ . Figure of merit is an indirect measurement of a material's thermoelectric efficiency; its ability to convert a thermal heat flux to electrical power, and vice versa. Material  $zT$  has been limited to approximately 1 since the 1950's; in the past decade there have been several reports of  $zT > 1.4$ . The major drawback for the development of thermoelectric devices is historically low material efficiency. However, it has been predicted that only a  $zT = 2$  is necessary to reach widespread usage of thermoelectric materials. A high  $zT$  material requires high thermopower, low electrical resistivity, and low thermal conductivity. These three material parameters are all interrelated. Therefore, recent research has focused on decoupling these parameters from each other.

In this thesis, the underlying theory that is necessary for characterizing thermoelectric materials is outlined. We investigate the  $zT$  increase in the material system PbTe-PbS that was achieved through nanoprecipitation of PbS rich regions in a bulk PbTe matrix. After performing a full galvanomagnetic and thermomagnetic characterization where electrical resistivity, Seebeck, Hall, and Nernst-Ettingshausen coefficients are measured we calculate Fermi level, carrier effective mass, and scattering parameter. The introduction of the second phase of PbS in PbTe does not lower the product  $S^2\sigma$  but is reported to

reduce thermal conductivity. It is this decrease in thermal conductivity that leads to a gain in  $zT$ .

The second system studied is  $\text{Bi}_2\text{Te}_3:\text{Sn}$ . It has been reported by Kulbachinskii that Sn possibly forms a resonant level in  $\text{Bi}_2\text{Te}_3$ , and in this thesis, we investigate this claim further. In order to do so, we calculate a Seebeck coefficient vs. carrier density (Pisarenko relation) for  $\text{Bi}_2\text{Te}_3$  and confirm it with experimental and literature data. This relation is necessary to determine if one has modified the density of states of  $\text{Bi}_2\text{Te}_3$  and increased thermopower over that of a similarly doped  $\text{Bi}_2\text{Te}_3$  that has a normal energy dispersion relation. In addition to the galvanomagnetic and thermomagnetic measurements, Shubnikov-de Haas (SdH) measurements are performed at 1.9K. There is conflicting literature on possible interpretations of the SdH measurements, we follow both interpretations and report the results. In summary, we conclude that by doping  $\text{Bi}_2\text{Te}_3$  to higher carrier densities, we could begin to dope the lower valence band thus leading to an increase in  $zT$ .

## VITA

April 29, 1985.....Born – Lorain, Ohio

2007.....B.S. Mechanical Engineering

2007-present.....Graduate Research Associate,  
The Ohio State University

## PUBLICATIONS

### Research Publications

1. L. Headings, Marano, V and Jaworski, C. (IMECE '06), Chicago, Illinois, Nov. 2006.
2. L. Headings, G. Washington, and C. Jaworski. Proc. SPIE, Vol. 6930, 69300C (2008)
3. J. Heremans and C. Jaworski. Applied Physics Letters, Volume 93, Issue 12, (2008)

## TABLE OF CONTENTS

ABSTRACT.....	ii
VITA.....	iv
TABLE OF CONENTS.....	v
LIST OF FIGURES .....	vii
LIST OF TABLES.....	x
1) INTRODUCTION TO THERMOELECTRICITY .....	1
Seebeck, Peltier, Thomson Effects and the Thomson Relations.....	1
Magnetic Field Induced Phenomena.....	3
Thermoelectric Devices .....	8
Overview of Thermoelectric Materials .....	11
2) EXPERIMENTAL TECHNIQUES .....	21
Material Preparation and Sample Mounting Procedures .....	21
Error Estimation.....	24
3) GENERAL THEORY .....	26
4 Parameter Fits – Non-Degenerate Case .....	27
4 Parameter Fits – Degenerate Case .....	32
Electronic Two Carrier Fits .....	33
Ambipolar Thermal Conductivity and the Wiedemann-Franz Law .....	34
Shubnikov-de Haas Oscillations and the Fermi Surface.....	37
4) LEAD TELLURIDE LEAD SULFIDE.....	44
Introduction.....	44
Measurements and Discussion.....	47
5) BISMUTH TELLURIDE .....	54
Introduction.....	54
Pisarenko Relation for P-Type Bismuth Telluride.....	56
Bismuth Tin Telluride.....	58
Literature Review.....	58
Experimental.....	59
Shubnikov-de Haas .....	60

Experimental Measurements and Interpretation of Transport Data at Low Magnetic Fields	65
Foundation for Increase in Thermopower in Bismuth Tin Telluride .....	71
6) CONCLUSION .....	74
WORKS CITED .....	75

## LIST OF FIGURES

Figure 1: Pictorial of the intuitive reason behind the Nernst effect. Note that in this image, holes are the majority carrier. Diffusing electrons (or holes) are deflected differing amounts by the magnetic field and set up a transverse electric field. ....	6
Figure 2: The fundamental unit of a thermoelectric generator. It consists of p-type and n-type legs that are connected thermally in parallel and electrically in series. A heat flux, $Q_h$ , enters the hot side at $T_{hot}$ . Further, $Q_c$ exits at $T_{cold}$ . This temperature difference creates a voltage due to the Seebeck effect. When connected to a load resistance, current flows and electrical power is generated. ....	9
Figure 3: Material efficiency divided by Carnot efficiency for the same hot and cold side temperatures as function of $zT$ for $\Delta T = 200K, 400K, 600K$ . This plot can be obtained from (1.15). ....	10
Figure 4: Summary of High $zT$ materials. From Refs (9:13). ....	12
Figure 5: Plot depicting the relation between Seebeck coefficient and electrical conductivity. An optimum doping level at each temperature can be found to maximize the product $S^2\sigma$ . ....	14
Figure 6: Dispersion relation in a parabolic band and the density of available states $g(E)$ as a function of energy. The dotted line is in a normal material and the solid line exhibits the characteristic spike in density of available states that a material with a resonant level possesses (11) ....	18
Figure 7: Schematic illustrating how a spike in the density of states (DOS) that is properly positioned can increase a material's thermopower. ....	19
Figure 8: Electronic density of states for different dimensional material. A bulk 3-D material system has a continuous function; 2-D, a step function. Removing another dimension results in a delta function with an exponential decay, and a 0-D system has a delta function shaped density of states. ....	20
Figure 9: Schematic of tested sample. A transverse magnetic field, $B$ , is passed through the sample. Two copper-constantan thermocouples ( $T_H$ , $T_C$ ) provide temperature measurement and also function as voltage leads. The longitudinal measurements (Seebeck coefficient, electrical resistivity, thermal conductivity) are made using $T_H$ and $T_C$ for temperatures and the copper lead of $T_H$ and $T_C$ for voltage. Current is passed through $I+$ and $I-$ . Transverse measurements (Nernst and Hall) are taken with the copper leads of $T_H$ and $V_T$ . A second set is taken using $T_C$ and $V_B$ for comparison. ....	21
Figure 10: Schematic of ambipolar conductivity. The circulating electron and hole fluxes create an extra Peltier heat flux yet no net additional electrical current. ....	36
Figure 11: Fermi surface of a constant energy sphere. The magnetic orbit (shaded section) is the intersection of the Fermi surface with a plane normal to the magnetic field. The location of the intersection of the magnetic field and the Fermi surface changes as the magnetic field varies. ....	38
Figure 12: Geometry of quantization of orbits. With a small change in energy $\Delta E$ , a distance $\Delta k$ is moved in $k$ -space. The integral around the new ellipse in $k$ -space is proportional to $\Delta A$ . This allows for the relation between the cyclotron frequency and $\Delta E/\Delta A$ . ....	40



Figure 13: At zero field, the Fermi surface is a sphere. However, a magnetic field forces a re-quantization of the Fermi surface into 'tubes' of varying energies.....	41
Figure 14: Schematic of the magnetic field quantized density of states in the direction perpendicular to the field. As the field is increased, the available states increase in energy and pass through the Fermi level. This creates the oscillations that appear in 1/magnetic field. ....	42
Figure 15: Phase diagram for the PbTe-PbS system. Pure PbS is on the left; PbTe the right. It is in the miscibility gap (non shaded region) that PbS rich regions are precipitated out of the PbTe matrix. As the anneal is at 500 °C, the matrix has the approximate composition $\text{PbTe}_{95}\text{S}_5$ . <sup>(22)</sup> ...	45
Figure 16: SEM image of PbTe-PbS showing nanoinclusions of PbS prepared at OSU. It is believed that these inclusions scatter phonons and not electrons, thus decreasing thermal conductivity without adversely affecting electrical resistivity. The PbS dots are 30-50 nm in diameter. ....	46
Figure 17: Galvanomagnetic (resistivity $\rho$ and Hall coefficient $R_H$ ) and thermomagnetic (Seebeck S and isothermal transverse Nernst N coefficients) data as a function of temperature for the samples studied. The points indicate the measured data, while the lines represent the recalculated properties using the calculated values for Fermi Energy, carrier density, effective mass, and scattering parameter. The symbols are: (●) $(\text{PbTe})_{96}(\text{PbS})_4$ , (▲) $(\text{PbTe})_{92}(\text{PbS})_8$ , (■) $(\text{PbTe})_{84}(\text{PbS})_{16}$ , (◆) $(\text{PbTe})_{70}(\text{PbS})_{30}$ . ....	48
Figure 18: Seebeck coefficient against carrier density at 300K. The solid curve is the Pisarenko relation for bulk PbTe. We note that all samples in this series fall below the curve. The symbols are: (●) $(\text{PbTe})_{96}(\text{PbS})_4$ , (▲) $(\text{PbTe})_{92}(\text{PbS})_8$ , (■) $(\text{PbTe})_{84}(\text{PbS})_{16}$ , (◆) $(\text{PbTe})_{70}(\text{PbS})_{30}$ . ....	49
Figure 19: Power factor and carrier density as functions of temperature. A similarly doped PbTe is included in the power factor plot for comparison. The symbols are: (●) $(\text{PbTe})_{96}(\text{PbS})_4$ , (▲) $(\text{PbTe})_{92}(\text{PbS})_8$ , (■) $(\text{PbTe})_{84}(\text{PbS})_{16}$ , (◆) $(\text{PbTe})_{70}(\text{PbS})_{30}$ . ....	50
Figure 20: Summary of 4-parameter fit on the PbTe/PbS system. The symbols are: (●) $(\text{PbTe})_{96}(\text{PbS})_4$ , (▲) $(\text{PbTe})_{92}(\text{PbS})_8$ , (■) $(\text{PbTe})_{84}(\text{PbS})_{16}$ , (◆) $(\text{PbTe})_{70}(\text{PbS})_{30}$ . (+) $\text{Pb}_{95}\text{Sn}_5\text{Te}$ . We note the decrease in effective mass of the PbTe-PbS system compared to standard $\text{PbSnTe}$ . Additionally, the scattering parameter is greatly increased, ranging from 1.5-3.5 at 300K. ....	51
Figure 21: Brillouin zone for $\text{Bi}_2\text{Te}_3$ containing the location of symmetry points. <sup>(26)</sup> .....	55
Figure 22: Pisarenko relation for p-type $\text{Bi}_2\text{Te}_3$ as calculated at 300K. The solid line represents the calculation. The symbols are (+) $\text{Bi}_2\text{Te}_3\text{:Sn}$ as reported in this thesis, (◆) $\text{Bi}_2\text{Te}_3$ doped with $\text{Pb}^{(32)}$ , (▼) $\text{Bi}_2\text{Te}_3\text{:Sn}$ with other Sn concentrations <sup>(33)</sup> , (▲) $\text{Bi}_2\text{Te}_3$ doped with $\text{Ge}^{(32)}$ , (✕) $\text{Bi}_2\text{Te}_3$ with Tl and Bi impurities as measured by this author, (□) off-stoichiometric $\text{Bi}_2\text{Te}_3$ <sup>(24)</sup> . The data points represent this author's own measurements as well as a collection of literature data. ....	57
Figure 23: Schematic of valence band energy levels for $\text{Bi}_2\text{Te}_3$ and $\text{Bi}_{2-x}\text{Sn}_x\text{Te}_3$ from Ref. (33). The impurity tin state band is located 15 meV below the top of the upper valence band.....	59
Figure 24: SdH oscillations for the three alloys. The curves have been shifted on the y-axis for ease of viewing. The symbols are: (solid line), $\text{Bi}_{1.9975}\text{Sn}_{0.0025}\text{Te}_3$ (dashed line) $(\text{Bi}_{1.9925}\text{Sn}_{0.0075}\text{Te}_3)$ , (dotted line) $\text{Bi}_{1.985}\text{Sn}_{0.015}\text{Te}_3$ . ....	61
Figure 25: The symbols are (●) $\text{Bi}_{2-x}\text{Sn}_x\text{Te}_3$ from (33), (○) $\text{Bi}_2\text{Te}_3$ from (29), (□) $\text{Bi}_{2-x}\text{Sn}_x\text{Te}_3$ from this work. The solid line is the calculated curve for $\text{Bi}_2\text{Te}_3$ from (29). We note the deviation from the line at 15 meV for Kulbachinskii and 23 meV for Kohler. ....	64

Figure 26: Galvanomagnetic (resistivity $\rho$ and Hall coefficient $R_H$ ) and thermomagnetic (Seebeck $S$ and isothermal transverse Nernst ( $N$ ) coefficients) data as a function of temperature for the samples studied. The points indicate the measured data, while the lines are added to guide the eye. The symbols are: (+) $\text{Bi}_{1.9975}\text{Sn}_{0.0025}\text{Te}_3$ , (◆) $\text{Bi}_{1.9925}\text{Sn}_{0.0075}\text{Te}_3$ , (●) $\text{Bi}_{1.985}\text{Sn}_{0.015}\text{Te}_3$ .....	66
Figure 27: Power factor on the left and hole carrier densities for the alloys. Note the symbols are: (+) $\text{Bi}_{1.9975}\text{Sn}_{0.0025}\text{Te}_3$ , (◆) $\text{Bi}_{1.9925}\text{Sn}_{0.0075}\text{Te}_3$ , (●) $\text{Bi}_{1.985}\text{Sn}_{0.015}\text{Te}_3$ .....	67
Figure 28 : Summary of four parameter fit using the degenerate equations. A pure $\text{Bi}_2\text{Te}_3$ sample is included for reference; however, this sample has a higher doping level, which is reflected in a smaller mobility and higher Fermi level at low temperature. Note the symbols are: (+) $\text{Bi}_{1.9975}\text{Sn}_{0.0025}\text{Te}_3$ , (◆) $\text{Bi}_{1.9925}\text{Sn}_{0.0075}\text{Te}_3$ , (●) $\text{Bi}_{1.985}\text{Sn}_{0.015}\text{Te}_3$ .....	68
Figure 29: These plots show the total thermal conductivity and $zT$ for the $\text{Bi}_{2-x}\text{Sn}_x\text{Te}_3$ samples. Note that these samples have radiative heat loss errors that cannot be corrected. Increasing tin concentration shifts the peak $zT$ to the right. Note the symbols are: (+) $\text{Bi}_{1.9975}\text{Sn}_{0.0025}\text{Te}_3$ , (◆) $\text{Bi}_{1.9925}\text{Sn}_{0.0075}\text{Te}_3$ , (●) $\text{Bi}_{1.985}\text{Sn}_{0.015}\text{Te}_3$ .....	69
Figure 30: Lorenz number over free electron Lorenz number on the left and electronic thermal conductivity as calculated from the Lorenz number and electrical resistivity. Note the symbols are: (+) $\text{Bi}_{1.9975}\text{Sn}_{0.0025}\text{Te}_3$ , (◆) $\text{Bi}_{1.9925}\text{Sn}_{0.0075}\text{Te}_3$ , (●) $\text{Bi}_{1.985}\text{Sn}_{0.015}\text{Te}_3$ .....	70
Figure 31: Total, lattice, electrical, and ambipolar thermal conductivity for $\text{Bi}_{1.9975}\text{Sn}_{0.0025}\text{Te}_3$ . The symbols are: (✕) total thermal conductivity, (▲) lattice, (●) electronic, and (□) ambipolar.....	70
Figure 32: Plot of Seebeck for $x=0.0025, 0.0075$ samples at lower temperatures on a log-log scale. The symbols are (+), $\text{Bi}_{1.9975}\text{Sn}_{0.0025}\text{Te}_3$ (◆) $\text{Bi}_{1.9925}\text{Sn}_{0.0075}\text{Te}_3$ , and the $T^1$ trace to (0,0) from the peak Seebeck and corresponding temperature for $\text{Bi}_{1.9975}\text{Sn}_{0.0025}\text{Te}_3$ . This trace is calculated for $m_D^*$ from UVB and $\lambda=3/2$ . ....	72
Figure 33: Pisarenko relation for $\text{Bi}_2\text{Te}_3$ as calculated for 260 K. We note that these samples fall far above the line. Note the symbols are: (+) $\text{Bi}_{1.9975}\text{Sn}_{0.0025}\text{Te}_3$ , (◆) $\text{Bi}_{1.9925}\text{Sn}_{0.0075}\text{Te}_3$ , (●) $\text{Bi}_{1.985}\text{Sn}_{0.015}\text{Te}_3$ .....	73

## LIST OF TABLES

Table 1: Properties of PbSnTe-PbS alloys studied at 300K. the carrier density $n$ is given in column 2, then electrical mobility $\mu$ , Hall coefficient $R_H$ , resistivity $\rho$ , Seebeck coefficient $S$ , power factor ( $P=S^2\sigma$ ), Nernst coefficient $N$ , scattering parameter $\lambda$ , and density of states effective mass $m^*$ . .....	53
Table 2. Tin concentrations and magnetic field oscillation frequencies and the corresponding Fermi surface areas for the three tested alloys. From Eq. (3.45) .....	60
Table 3: Material parameters that have been calculated using the SdH measurements following the Kohler method. <sup>(30)</sup> Note that the density of states effective mass in the second band becomes increasingly large with increasing carriers in the second band. Refer to Figure 25. ....	64

## 1) INTRODUCTION TO THERMOELECTRICITY

### Seebeck, Peltier, Thomson Effects and the Thomson Relations

The study of thermoelectric phenomena and the usage of thermoelectric material in direct energy conversion devices have its origins in 1821 when Thomas Seebeck discovered what has since been labeled the Seebeck effect. He found that when two dissimilar conductors are joined with one junction heated and the other kept cool a voltage differential is created. This occurs because an individual material can create a voltage difference between its ends when there is a temperature difference across it. This is labeled a material's Seebeck coefficient and is defined as:

$$S = \frac{\vec{E}}{\nabla T} = \frac{\Delta V}{\Delta T} \quad (1.1)$$

This phenomenon arises because the temperature differential causes the majority carrier to diffuse to the cold side of the material, thus charging that side positive or negative, depending on whether the carriers are holes or electrons. The hot side takes the opposite charge, and a potential difference is created. Note that the Seebeck coefficient of a junction is the difference between the Seebeck coefficients of the two materials. Metals typically have a small Seebeck Coefficient at room temperature, less than  $5 \mu\text{V/K}$ , whereas semimetals have higher values, for example, Bismuth has a value of  $-66 \mu\text{V/K}$ . In semiconductors and oxides these values can reach up to several hundred  $\mu\text{V/K}$ .

The Peltier effect occurs upon the passage of an electrical current through a junction of dissimilar metals at temperature  $T$ . Heat is absorbed or released at the junction depending on the sign of the current. This heat is superimposed on that of  $I^2R$  joule heating. We define the Peltier Coefficient  $\Pi$  as:

$$q = I \cdot \Pi \quad (1.2)$$

where  $q$  is the heat flow and  $I$  is the electrical current. It can be shown as the first Kelvin relation that the Seebeck and Peltier coefficients of a material are related by:

$$\Pi = S \cdot T \quad (1.3)$$

where  $T$  is the absolute temperature of the material at the point of contact.

The Thomson effect was discovered by Lord Kelvin, who also determined the relations between the three thermoelectric effects. An electric current flowing through a homogeneous conductor with a temperature gradient superimposed releases or absorbs energy based on the direction of their travel as determined by:

$$q_{Thomson} = \tau \cdot I \cdot (-\Delta T) \quad (1.4)$$

where  $\tau$  is the Thomson coefficient. The existence of the Thomson effect is due to the temperature dependence of the Seebeck coefficient in a material. The Seebeck and Thomson coefficients are related by:

$$\tau = T \frac{\partial S}{\partial T} \quad \& \quad S = \int_0^T \frac{\tau}{T} dT \quad (1.5)$$

This effect occurs because the entropy of a charge carrier is temperature dependant. It is this entropy variation that changes the amount of heat carried by the charges and thus leads to the evolution or absorption of heat. Additionally, in the absence of a temperature gradient,  $q_{Thomson} = 0$ . The second Thomson relation is:

$$\tau_A - \tau_B = T \frac{\partial \alpha_{AB}}{\partial T} = T \frac{\partial \alpha_A}{\partial T} - T \frac{\partial \alpha_B}{\partial T} \quad (1.6)$$

This relation allows for the direct measurement of a material's Seebeck effect. The measurement is possible by connecting the material in series with a superconductor, as the Seebeck of a superconductor in its superconducting range is zero. It is zero because the charge carriers do not carry entropy. Above superconducting temperatures, the Thomson coefficient can be measured using (1.4) and Seebeck can be calculated using (1.5). This has been performed on lead<sup>(1)</sup>. Therefore, the direct measurement of any material's Seebeck is possible by connecting it to lead.

## **Magnetic Field Induced Phenomena**

Four important effects in the measurement and characterization of thermoelectric (TE) materials are magnetoresistance, magnetoseebeck, the Hall effect, and the Nernst-Ettingshausen (Nernst) effect. These phenomena are due to the interaction of the electronic structure of materials with a magnetic field. In this discussion, we will refer to the carriers as electrons; it can be shown that the same equations hold for holes.

The Hall effect occurs in a material when a current with density  $j_x$  flows at a right angle to an applied magnetic field  $B_z$ . The created electric field  $E_y$  is proportional to the Lorenz force  $j_x B_z$  with the constant of proportionality defined as the Hall coefficient  $R_H$ :

$$E_y = R_H j_x B_z \quad (1.7)$$

with units of Ohm-meter/Tesla.<sup>(1)</sup> In a single carrier system with cubic crystal symmetry and parabolic bands, this equation allows for the direct measurement of the number of charge carriers and their sign. If one considers a single electron traveling with velocity  $\mathbf{v}$ , this electron will experience the Lorentz force  $(\mathbf{B} \times \mathbf{v}) \cdot q$ , where  $q$  is the electron charge. As this electron is confined within a solid, it will be deflected in a direction perpendicular to  $B_z$ . As more electrons are deflected, they create a counterimposing electric field that will balance the Lorentz force on the bulk of the carriers, which will flow as before. This gives the magnetic generated electric field as  $(\mathbf{B} \times \mathbf{v}) \cdot q = E_y \cdot q$ . With the same orientation as (1.7),  $j_x = n \cdot q \cdot v$ , where  $n$  is the carrier density. Further manipulation

yields  $E_y = -\frac{1}{n \cdot q} j_x B_z$  and a convenient expression for the Hall coefficient:

$$R_H = -\frac{A}{n \cdot q} \quad (1.8)$$

As a first approximation,  $A$  can be taken to be unity and the Hall coefficient is thus a direct measurement of carrier density. This sign convention yields a negative Hall coefficient when electrons are the majority carrier. This simple modeling does not address two carrier systems or the prefactor  $A$  on the right hand side that addresses the band structure's and the scattering parameter's impacts on the Hall coefficient. These will be discussed in Section 3.

Another phenomenon of interest is magnetoresistance. This is defined as:

$$MR(B) = \frac{\rho(B) - \rho(0)}{\rho(0)} \quad (1.9)$$

The mechanisms creating magnetoresistance are as follows. Conduction electrons have a distribution of velocities that is given by the Maxwell-Boltzmann distribution. As the Hall field compensates for the mean velocity of electrons, electrons with faster and slower velocities will undergo deviations from rectilinear paths. This leads to the decrease in free path length for these electrons and an increase in resistance. Additionally, if both holes and electrons contribute to the conduction process, i.e. two carrier conduction, the Hall effect cannot compensate their deflections in a magnetic field. This causes the direction dependence of the carriers' momentum vector to depart from a spherical shape. The energy of conducting electrons depends on direction, with this dependence increasing at lower temperatures. Therefore, at low temperatures, this dependence gives a strong dependence of the resistivity upon the magnetic field and its orientation to the crystallographic direction. The magnetoresistance of a material is most pronounced at low temperatures. Additionally, a two carrier system will exhibit a higher magnetoresistance than a corresponding single carrier system.

Next, we address the Nernst-Ettingshausen effect (Nernst effect). With  $dT/dx$ , there is a flux of diffusing carriers. They move with a drift velocity  $v_{dif}$  and in a perpendicular magnetic field are deflected by the Lorentz force. This creates an electric field  $E_y$  like in the Hall effect. The Nernst coefficient  $N$  is defined in the relation:

$$E_y = N \cdot B_z \frac{dT}{dx} \quad (1.10)$$



This effect is depicted in Figure 1. A temperature gradient causes the diffusion of the majority carrier from the hot to cold side. As the velocities of diffusing electrons are statistically distributed, the slow electrons are deflected further by a magnetic field than the fast electrons due to the amount of time that they take to traverse the solid. As a result, a transverse voltage is setup to balance out the electric field created by the Lorentz force. The Nernst coefficient is a direct measurement of the dominant scattering mechanism, because it measures the energy distribution of drift velocities.

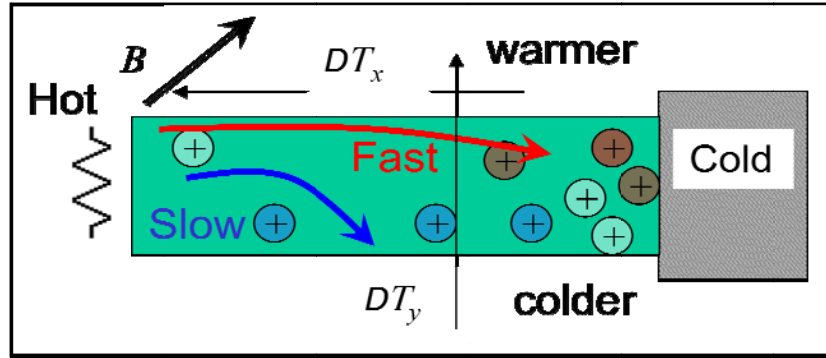


Figure 1: Pictorial of the intuitive reason behind the Nernst effect. Note that in this image, holes are the majority carrier. Diffusing electrons (or holes) are deflected differing amounts by the magnetic field and set up a transverse electric field.

As the measured Nernst coefficient is the adiabatic coefficient (heat flow in the transverse direction is zero), a correction factor needs to be applied to convert it to the isothermal Nernst, which is needed for use in the data treatment as discussed in Section 3. This Nernst coefficient  $N_{iso}$  is measured with the temperature difference along the transverse direction of zero.  $N_{iso}$  is found by multiplying the measured Nernst coefficient  $N_a$  by the following correction factor<sup>(2)</sup>:

$$NiNa = \left( 1 + \frac{7q}{4k_B} \frac{|S|L_0}{\nu\kappa} T \right)^{-1} \quad (1.11)$$

The Nernst  $N$  used henceforth is the isothermal Nernst  $N_{\text{iso}}$

## Thermoelectric Devices

Next, we move into the analysis of a thermoelectric device. For simplicity, we skip the lengthy derivations as well as contact losses and consider only thermoelectric generators; however, it is easy to derive similar relations for thermoelectric heat pumps. For a full development, consult with several related texts.<sup>(3)(4)</sup> In Figure 2, we see a typical TE couple that consists of one p-type and one n-type leg that are connected electrically in series, thermally in parallel. Assuming equal size n-type and p-type legs, the heat entering the hot side  $Q_h$  is comprised of three elements:

$$Q_h = \kappa \frac{A}{L} \Delta T + S \cdot I \cdot T_H - \frac{1}{2} I^2 R \quad (1.12)$$

where  $\kappa$  is the thermal conductivity of the material,  $A$  and  $L$  are the leg's area and length,  $\Delta T$  is the temperature difference,  $I$  is the electrical current and  $R$  is the resistance of the leg. The first term stems from thermal conduction through the leg, the second from Peltier heat, and the last from Joule heating. Note that this term is negative as half of the Joule heating reaches the hot side. Correspondingly, the heat exiting the cold side is

$$Q_c = K \frac{A}{L} \Delta T + S \cdot I \cdot T_C + \frac{1}{2} I^2 R \quad (1.13)$$

Output power can be expressed as  $P_{gen} = I^2 R_{load}$  and efficiency as

$$\eta = \frac{I^2 R_{load}}{K \frac{A}{L} \Delta T + S \cdot I \cdot T_H - \frac{1}{2} I^2 R} \quad (1.14)$$

The couple's leg areas and lengths, along with the output resistance, can be varied to give the optimum power or efficiency. Maximum power is reached when  $R_{\text{load}} = R_{\text{module}}$ . Further, maximum theoretical efficiency  $\eta$ , is described by:

$$\eta_{\text{max}} = \frac{\Delta T}{T_H} \left[ \frac{\sqrt{zT+1}-1}{\sqrt{zT+1} + \frac{T_H}{T_C}} \right] \quad (1.15)$$

where  $z$  is the thermoelectric figure of merit:  $z = \frac{S^2 \sigma}{\kappa}$ ,  $\sigma$  is a material's electrical conductivity and  $\kappa$  is the thermal conductivity. It is this figure of merit multiplied by temperature ( $zT$ ) that in the thermoelectric community is the standard non-dimensional number for evaluation of material.

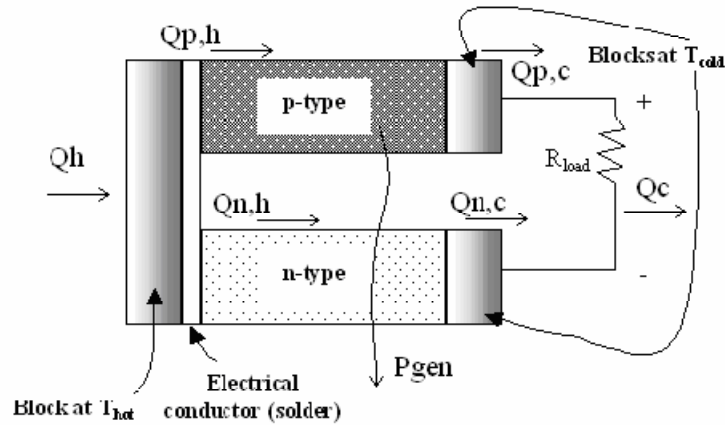


Figure 2: The fundamental unit of a thermoelectric generator. It consists of p-type and n-type legs that are connected thermally in parallel and electrically in series. A heat flux,  $Q_h$ , enters the hot side at  $T_{\text{hot}}$ . Further,  $Q_c$  exits at  $T_{\text{cold}}$ . This temperature difference creates a voltage due to the Seebeck effect. When connected to a load resistance, current flows and electrical power is generated.

Notice that the efficiency (1.15) is directly related to Carnot efficiency, and will be less than Carnot except in the limiting case  $zT = \text{infinity}$ . Figure 3 shows maximum efficiency as a portion of Carnot efficiency as a function of  $zT$ . Note that an increase in  $zT$  from 1 – 2 improves performance from 18% to 35% of Carnot efficiency while a  $zT=4$  only reaches 45% of Carnot efficiency for  $\Delta T=600\text{K}$ . Recently, Bell proposed a new thermal management scenario incorporating thermal isolation in a 'stack design' where thermal and electrical currents flow in the same direction.<sup>(5)(6)</sup> This new design has led to a reported doubling in device COP of heat pumps for the same thermoelectric  $zT$  and a reduction in the amount of thermoelectric material necessary due to its high power density.

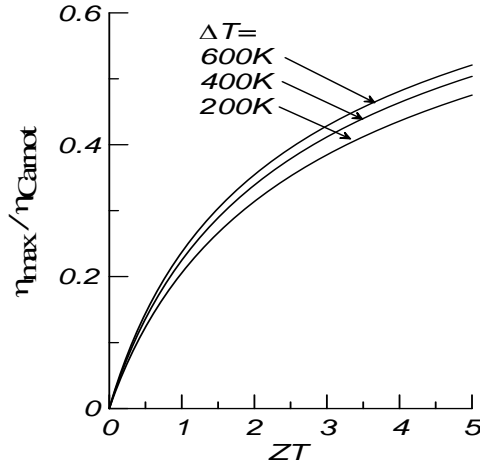


Figure 3: Material efficiency divided by Carnot efficiency for the same hot and cold side temperatures as function of  $zT$  for  $\Delta T=200\text{K}$ ,  $400\text{K}$ ,  $600\text{K}$ . This plot can be obtained from (1.15).

Further analyzing the dimensionless figure of merit:

$$zT = \frac{S^2}{\rho \cdot \kappa} T = \frac{S^2 \sigma}{\kappa} T \quad (1.16)$$

and the numerator is termed the power factor:

$$P = S^2 \sigma \quad (1.17)$$

We note that desirable materials have high thermopower and low electrical resistivity and thermal conductivity. This forces most good thermoelectric materials to be semiconductors that are heavily doped ( $10^{19}$ - $10^{20}$  carriers  $\text{cm}^{-3}$ ) for a maximum power factor (the numerator  $S^2 \sigma$ ). In order to keep thermal conductivity low, heavy atoms are chosen because they typically pack in large unit cells and have low specific heat per unit volume. It is important to note that while a material may have a peak  $zT$  at temperature  $T$ , its operating  $ZT$  is lessened as its  $zT$  must be integrated over the whole operating temperature range. A device's  $ZT$  is also lessened due to thermal and electrical contact losses. We note this significant distinction with lowercase  $z$  for a material's  $zT$  at one temperature  $T$ ; an uppercase  $Z$  delineates an integrated material  $zT$  that evaluates a device's performance<sup>(7)</sup>.

## Overview of Thermoelectric Materials

In the beginning of the 1950's, starting with the advent of semiconductor technology, a level of material purity was reached that allowed the systematic study of TE compounds. The early material systems identified were bismuth telluride ( $\text{Bi}_2\text{Te}_3$ ) and lead telluride ( $\text{PbTe}$ )<sup>(3)</sup>. About 30 years later, silicon germanium alloys were invented that worked at high temperatures and were installed in NASA space probes<sup>(3)</sup>. However, these materials all have a maximum  $zT$  less than 1 in their operating temperature ranges. There was not any major increase in  $zT$  until the early 2000's when several high  $zT$  values were reported on thin film and superlattice materials. In 2002, Harman reported high  $zT$  values

(reaching 3.2 at 300 °C) for quantum dot superlattices. Recently, we have seen reports of  $\text{Bi}_2\text{Te}_3/\text{Sb}_2\text{Te}_3$  superlattices with  $zT=2.4$  at 300K,<sup>(8)</sup> Lead Antimony Silver Telluride ( $\text{AgPbSbTe}$ ) with a reported  $zT=1.7$  at 700K,<sup>(9)</sup>  $\text{PbSbTe}$  with a reported  $zT$  of 1.4 at 700K,<sup>(10)</sup>  $\text{PbTe-PbS}$  with a reported  $zT=1.5$  at 640K,<sup>(11)</sup> and  $\text{PbTe:Tl}$  with a reported  $zT$  of 1.5 at 800K.<sup>(12)</sup> Refer to Figure 4 for a graph of high  $zT$  materials and their operating ranges compiled from Refs (9:13). Because  $zT$  involves measurement of at least three independent quantities, each with its own uncertainty, not all the claims for high  $zT$  in literature or in Figure 4 can be taken at face value without an in-depth study of materials variations (compiling measurements performed on different samples into one final  $zT$ ) and measurement techniques.

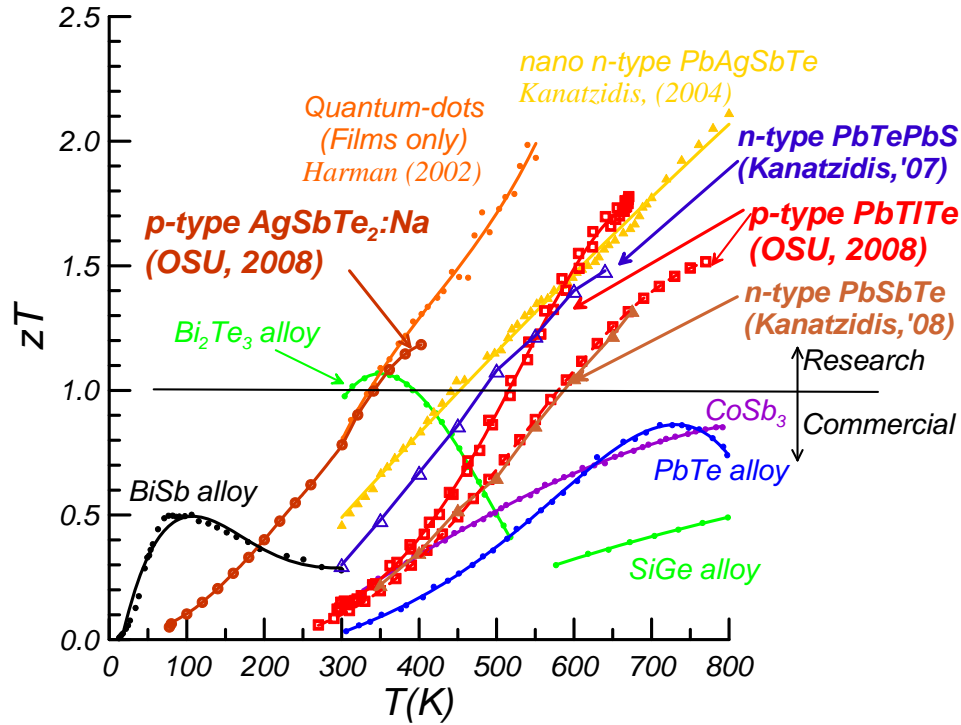


Figure 4: Summary of High  $zT$  materials. From Refs (9:13).

Before introducing theoretical methods to improve material  $zT$  it is important to better understand the two components thermal and electrical conductivity. Thermal conductivity is a sum of heat transported by phonons or the lattice thermal conductivity,  $\kappa_L$ , that of electrons or holes (electronic thermal conductivity),  $\kappa_e$ , electron-hole pairs in the intrinsic conduction region (ambipolar conduction),  $\kappa_{ambi}$ , and several other mechanisms (excitons, spin waves, and photons) that typically do not play a significant role in thermal conduction in thermoelectric material. The relative importance of each of these components depends on the material system as well as the doping degree and temperature range. The lattice thermal conductivity yields information on the presence of various defects in the lattice: vacancies, dislocations, charged or neutral impurities, etc. The electronic portion is related to the carrier scattering mechanism, electrical mobility, and carrier density. For the discussion into nanotechnology and thermoelectricity, it is useful to further explain the electronic thermal conductivity. Following a customary treatment, we can characterize the heat transported by electrons using the Wiedemann-Franz law  $\kappa_e = L \cdot \sigma \cdot T$  where  $L$  is the electron Lorenz number. For a free electron moving in vacuum, the free electron Lorenz number  $L_0 = \frac{\pi^2}{3} \left( \frac{k_b}{q} \right)^2 = 2.44 \cdot 10^{-8} W\Omega K^{-1}$ , but for electrons in a solid it is only ~60-90% of  $L_0$ . One must calculate the reduced Lorenz number for each material. The exact values depend on the Fermi level and scattering parameter. Assuming a free electron Lorenz number will result in incorrectly calculating the lattice portion of thermal conductivity. The Wiedemann-Franz law will be discussed further in Section 3.



The electrical conductivity of a solid is given by a well known formula  $j_x = \sigma \cdot E_x$ . This assumes one dimensional conduction; a two or three dimensional case can be represented with tensors. Further:

$$\sigma = q \cdot \mu \cdot n \quad (1.18)$$

where  $q$  is the electron charge,  $n$  is carrier density, and  $\mu$  is the electron mobility.

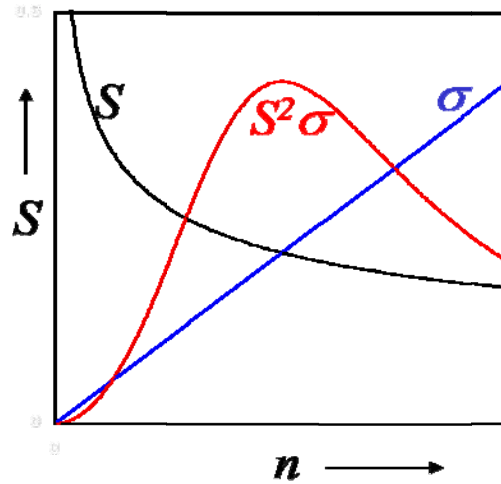


Figure 5: Plot depicting the relation between Seebeck coefficient and electrical conductivity. An optimum doping level at each temperature can be found to maximize the product  $S^2\sigma$ .

The mechanisms to improve  $zT$  can be divided into two areas. One is to increase the power factor ( $S^2\sigma$ ). The other is to reduce the thermal conductivity. When addressing power factor, it is important to realize that thermopower, carrier density, and electrical conductivity are all interrelated. Shown in Figure 5 is a plot relating these three material properties. We see a maximum in power factor ( $S^2\sigma$ ) at an optimum carrier density (at a given temperature  $T$ ).

Upon looking at the denominator of  $zT$ , we realize that a lower thermal conductivity increases  $zT$ . There are two methods for reducing this. One is the classic technique of alloy scattering. By the introduction of a chemically similar but atomically larger or smaller element into the material, the difference in atom size and electrochemical potential can scatter phonons more than electrons. Classic examples are  $\text{Pb}_{1-x}\text{Sn}_x\text{Te}$  and  $\text{PbSe}_x\text{Te}_{1-x}$  or  $\text{Bi}_{1-x}\text{Sb}_x\text{Se}_y\text{Te}_{1-y}$ . However, this alloying has the potential to reduce electrical conductivity more than thermal conductivity, such as in  $\text{Pb}_{1-x}\text{Sn}_x\text{Te}$ . The electrical conductivity reduction depends on the difference in electrochemical potential between the atoms. We investigate another material system that attempts to raise  $zT$  by lowering thermal conductivity in this thesis,  $\text{PbTe-PbS}$ . In this material system, however, spinodal decomposition and nucleation and growth create nanoscale morphology that may also lead to a further reduction in lattice thermal conductivity over that of alloy scattering and phonon-phonon processes. To understand the other method for reducing  $\kappa_L$ , popularized in recent years, requires further expansion of the components of  $zT$ . Electrical conductivity can be expressed as:

$$\sigma = \frac{nq^2 l_e}{(2m^* E_F)^{\frac{1}{2}}} \quad (1.19)$$

where  $l_e$  is the electronic mean free path,  $m^*$  is the electron effective mass, and  $E_F$  is the Fermi energy. The effective mass is the mass that an electron traveling through a solid appears to have due to its interaction with periodic potentials of the host atoms and the Fermi energy is the highest occupied energy level in a system at 0K. We can also express thermal conductivity as its sum of lattice and electronic components (assuming one carrier conduction):

$$\kappa = \kappa_{\text{Lattice}} + \kappa_{\text{Electronic}} = \frac{1}{3} C_v \nu_{\phi} \ell_{\phi} + LT\sigma. \quad (1.20)$$

where  $C_v$  is the material specific heat, and  $\nu_{\phi}$  and  $\ell_{\phi}$  are the phonon velocity and mean free path, respectively. Using these definitions, we obtain a new expression for  $zT$ :

$$zT = \frac{S^2 \sigma}{\kappa} T = \frac{S^2 \sigma}{\frac{1}{3} C_v \nu_{\phi} \ell_{\phi} + LT\sigma} T = S^2 n \left( \frac{1}{\left( \frac{\ell_{\phi}}{\ell_e} \right) \frac{C_v \nu_{\phi}}{3q^2 T} (2m^* E_F)^{\frac{1}{2}} + Ln} \right) \quad (1.21)$$

We see here that  $zT$  can be subdivided into three terms: 1)  $S^2 n$ , 2)  $\left( \frac{\ell_{\phi}}{\ell_e} \right)$ , 3)  $L \cdot n$ . If  $\kappa_e <$

$\kappa_L$ , then we see that  $zT$  would rely most on the ratio  $\left( \frac{\ell_{\phi}}{\ell_e} \right)$ . Since both  $\ell_{\phi}$  and  $\ell_e$  are on

the order of 1-50 nm, the introduction of nanometer sized length scales have the potential to dramatically increase  $zT$  as long as they scatter phonons more efficiently than electrons. This method has realized gains in  $zT$ , with reports on thin films and nanowires. Further, work by Kanatzidis's group on PbTe-PbS, PbSbTe, and AgPbSbTe indicate that nanodots, nanoinclusions, etc. work to effectively reduce thermal conductivity.<sup>(13)</sup>

If  $\kappa_e > \kappa_L$ , then we see that  $zT$  would be governed mostly by  $S$ , and therefore an increase in  $S$  would have the greatest effect on  $zT$ . With the Mott equation for thermopower of degenerately doped semiconductors:

$$S = \frac{\pi^2}{3} \frac{k_B}{q} k_B T \left\{ \frac{1}{n} \frac{dn(E)}{dE} + \frac{1}{\tau} \frac{d\tau(E)}{dE} - \frac{1}{m^*} \frac{dm^*(E)}{dE} \right\}_{E=E_F} \quad (1.22)$$

where  $k_B$  is Boltzmann's constant,  $q$  is the electric charge,  $E$  is energy and  $\tau$  is the relaxation time. We see three components to this formula. First, note that by increasing carrier density,  $n$ , Seebeck is decreased, and vice versa, as shown in Figure 5. For a given scattering mechanism, one can calculate the Seebeck of a given material at each carrier concentration. Additionally, when  $n \geq 10^{19} \text{ cm}^{-3}$ , Seebeck follows a  $T^1$  law and decreases to zero at 0K. This is in accordance with the definition of Seebeck as a measurement of entropy, as entropy goes to zero at 0K. However, other methods exist to increase thermopower for a given carrier density. A classic method is through ionized impurity scattering, which will change the relaxation time and therefore increase Seebeck at a given carrier density. A second method, put forward by Mahan and Sofo, and only recently experimentally observed by Heremans, is through the modification of the density of states.<sup>(12)(14)</sup> This is most easily done through the introduction of a sharp band into the density of states, thereby increasing the effective mass and maximizing  $\frac{dn(E)}{dE}$ . This is depicted in Figure 6.

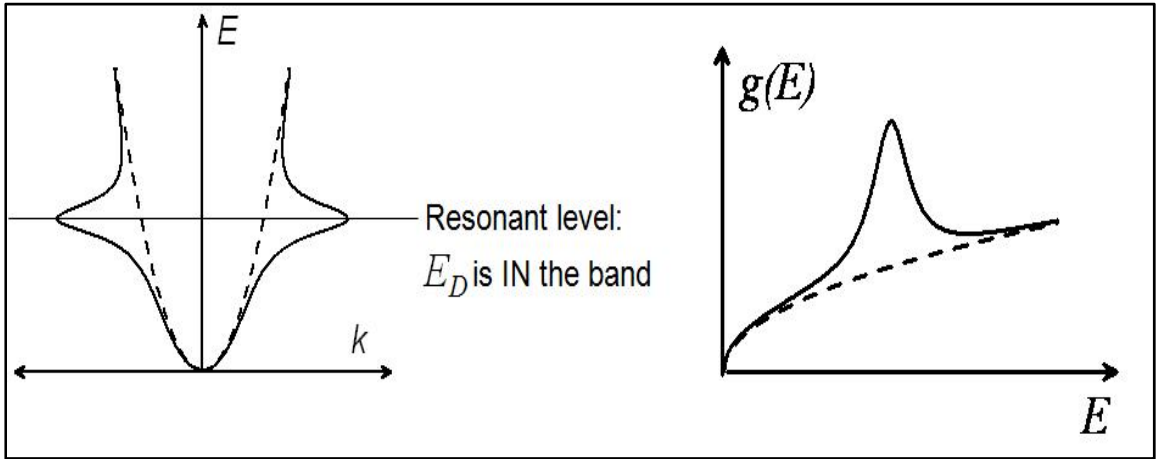


Figure 6: Dispersion relation in a parabolic band and the density of available states  $g(E)$  as a function of energy. The dotted line is in a normal material and the solid line exhibits the characteristic spike in density of available states that a material with a resonant level possesses<sup>(11)</sup>.

Figure 7 illustrates how resonant levels work. With Fermi-Dirac statistics given by:

$$f_0(E) = \frac{1}{1 + e^{\frac{E - E_F}{k_B T}}} \quad , \quad (1.23)$$

the cold end of the material will have a slightly sharper drop in  $f(E)$  than the hot end, as depicted in 7a. 7b shows the standard 3D density of states as a function of energy  $E$ . In 7c, the number of the electrons at the cold and hot end of the sample is shown as functions of energy. We see that the difference in total energy is small. However, with a spike in the density of states (7d) at the proper position the difference in energies between hot and cold ends is greatly increased (7e). This modification of density of states has been accomplished through the introduction of thallium to lead telluride.<sup>(12)</sup> In this thesis, the creation of a resonant level in  $\text{Bi}_2\text{Te}_3$  through doping with tin is investigated.

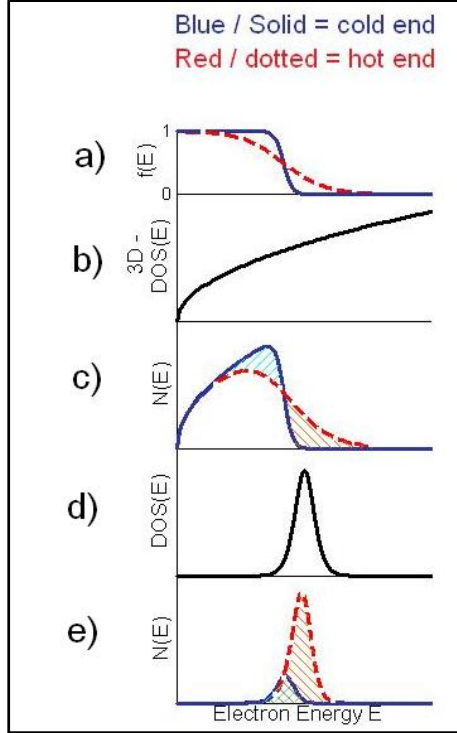


Figure 7: Schematic illustrating how a spike in the density of states (DOS) that is properly positioned can increase a material's thermopower.

Another method to achieve this spike in the density of states is size quantization. This was initially proposed by Hicks and Dresselhaus and experimentally confirmed by Heremans with bismuth nanowires.<sup>(15)(16)</sup> This method removes dimensions from a material thus creating spikes in the density of states. This is done through quantum wires, wells, and dots, the impact of which is shown in Figure 8. Heremans achieved an increase in thermopower by several orders of magnitude. Nanostructures are also capable of increasing Seebeck by filtering electrons according to their energies. From the point of view of the DOS, a resonant level can be viewed as the superposition and broadening of a 0-D quantum dot onto a 3-D density of states. This broadening is important because while a 0-D quantum dot will have infinite Seebeck, it will also have infinite resistivity.<sup>(17)</sup>

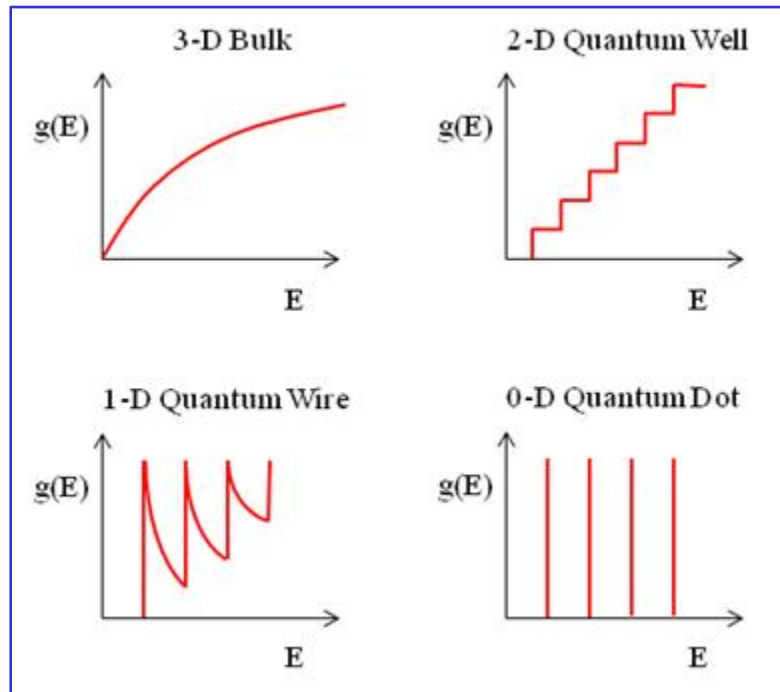


Figure 8: Electronic density of states for different dimensional material. A bulk 3-D material system has a continuous function; 2-D, a step function. Removing another dimension results in a delta function with an exponential decay, and a 0-D system has a delta function shaped density of states.

## 2) EXPERIMENTAL TECHNIQUES

### Material Preparation and Sample Mounting Procedures

Materials that are 5N or better purity are combined in a quartz ampoule in stoichiometric amounts measured to 10  $\mu\text{g}$  accuracy. After sealing in a vacuum at  $10^{-6}$  torr, the ampoule is placed in a furnace and heated to temperatures above the melting points of the elements. The materials then received different heat treatments that will be discussed further in the individual sections.

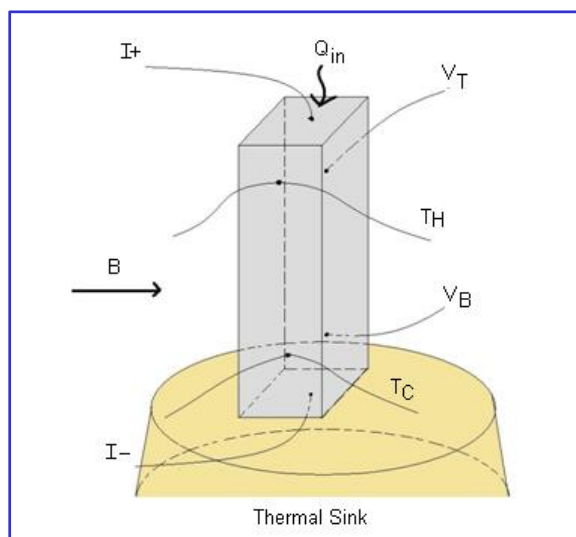


Figure 9: Schematic of tested sample. A transverse magnetic field,  $B$ , is passed through the sample. Two copper-constantan thermocouples ( $T_H$ ,  $T_C$ ) provide temperature measurement and also function as voltage leads. The longitudinal measurements (Seebeck coefficient, electrical resistivity, thermal conductivity) are made using  $T_H$  and  $T_C$  for temperatures and the copper lead of  $T_H$  and  $T_C$  for voltage. Current is passed through  $I+$  and  $I-$ . Transverse measurements (Nernst and Hall) are taken with the copper leads of  $T_H$  and  $V_T$ . A second set is taken using  $T_C$  and  $V_B$  for comparison.



Parallelepipeds measuring approximately 1 x 1 x 6mm are cut from the samples, using a diamond saw, for galvanomagnetic and thermomagnetic testing. A thin copper pad is silver epoxied to one end of the sample and acts as a current lead. This pad is attached with epoxy to an alumina pad which functions as a heat sink. Heat flux is established by using a resistive heater. Voltages are measured by copper wires that are 0.001” diameter and are spot welded to the sample. The top wire is used as a current lead and the other four function as voltage leads. Type T thermocouples are made by soldering a constantan wire to the spot where the copper wire contacts the sample. For added mechanical strength, silver epoxy is applied to the contacts. The thermocouples take differential measurements relative to the heat sink. The magnetic field is passed orthogonally to the current and heat fluxes. Refer to Figure 9.

Using these samples we simultaneously measure resistivity, Seebeck, Hall, and Nernst Coefficients. Measurements are taken at constant temperatures by sweeping magnetic fields between -1.5 to 1.5 Tesla. Resistivity is measured using the standard 4-wire AC method in order to cancel out the effects of the Seebeck voltage. The Hall coefficient is defined as the low magnetic field slope of the transverse Hall resistance ( $R_T=V_T/I$ ):

$$R_H = \frac{R_T \cdot t}{B} \quad (2.1)$$

where  $t$  is the thickness of the tested sample. The corresponding values for positive and negative Hall resistances  $R_T$  are averaged, thus canceling out geometric misalignment which creates magnetoresistance error<sup>(1)</sup>. Further, the Nernst coefficient is defined as the low magnetic field slope of the transverse voltage  $V_T$ , which arises by the simultaneous presence of a temperature gradient and magnetic field.

$$N = \frac{V_T \cdot L}{B \cdot W \cdot \Delta T} \quad (2.2)$$

where  $L$  and  $W$  are the length and width of the tested sample, respectively. Thermal conductivity measurements are split into two categories: high and low temperature. At low temperature (80-250K), the static heater and sink method is used. The same methodology is used as in the sample preparation on the parallelepipeds, but these samples have different dimensions. Samples with large surface area to height aspect ratio are used. Typical samples measure 3 x 3 x 1 mm. Higher temperature measurements require transient methods to eliminate the effects of radiative losses. In this case, thermal diffusivity  $\alpha$  and specific heat  $c_p$  are used to calculate  $\kappa$ .

$$\kappa = \rho \cdot \alpha \cdot c_p \quad (2.3)$$

where  $\rho$  is the density. Thermal diffusivity is measured using the flash thermal diffusivity method. The instrument which is used has a xenon flash lamp that illuminates one side of the sample with a short burst of radiant energy. A detector measures the resulting temperature rise of the rear surface and diffusivity values are calculated from temperature rise versus time. These measurements are from room temperature to 500 C. Specific heat is measured on a differential scanning calorimeter with the specific heat of sapphire as a reference using aluminum sample containers. Density is calculated at room temperature using the volume and mass of a sample and extrapolated to higher temperatures by using literature values for the coefficient of thermal expansion. It is then possible to interpolate between the low temperature and high temperature values to obtain data from 250-300 Kelvin using a radiative heat loss relation.

## Error Estimation

Seebeck coefficient errors are mostly attributed to the difficult task of measuring voltage and temperature at precisely the same location. Therefore, extreme care is taken to minimize the size of the contact, and thus heat draining capability. We estimate this error on the order of 3%. Other measurements of electrical resistivity, Hall and Nernst Coefficients, require measurement of the dimensions of the sample and are on the order of 5%. Thermal conductivity has the worst error, arising from several reasons. The flash diffusivity measurement is 10% accurate and the specific heat is accurate within 5%. For low temperature thermal conductivity, one must take into account radiation, area and length measurements, as well as heat from the heater that does not enter the sample. From these, error is estimated to also be 10%. As  $zT$  it is a product of these other terms, one would think that the error would be much higher, with the error  $\sigma_{zT}$  in  $zT$ :

$$\sigma_{zT} = \sqrt{\left(\frac{2S}{\rho \cdot \kappa}\right)^2 \sigma_S^2 + \left(\frac{S^2}{\rho^2 \cdot \kappa}\right)^2 \sigma_\rho^2 + \left(\frac{S^2}{\rho \cdot \kappa^2}\right)^2 \sigma_\kappa^2} \quad (2.4)$$

Typical values of a thermoelectric,  $S=80 \cdot 10^{-6} \mu\text{V/K}$ ,  $\rho=1.5 \cdot 10^{-5} \Omega\text{m}$ , and  $\kappa=2\text{W/mK}$ , yield an error of 16% in  $zT$ . However, upon breaking down  $zT$  into measured quantities, it is seen that certain quantities cancel each other out, thus yielding a lower error only if all the measurements, including thermal conductivity using the static method, are performed on the same sample at the same time. This reduction in error is only valid in the low temperature measurement:

$$zT = \frac{S^2}{\rho \cdot \kappa} T = \frac{\left[ \frac{V_s^2}{(T_H - T_C)^2} \right]}{\left[ R \frac{A}{L} \right] \cdot \left[ \frac{V_H \cdot I_H}{T_H - T_C} \frac{L}{A} \right]} T = \frac{\frac{V_s^2}{(T_H - T_C)}}{R \cdot V_H \cdot I_H} T = \frac{V_s^2 \cdot T}{(T_H - T_C) R \cdot V_H \cdot I_H} \quad (2.5)$$

Where  $V_s$  is the measured Seebeck voltage between the leads,  $P_H = V_H I_H$  is the input heater power,  $T_H - T_C$  is the temperature difference between hot and cold ends,  $R$  is the measured resistance, and  $T$  is the average temperature. We see that sample geometry is canceled out and the error is mostly based on the accuracy of the thermocouples and their contact resistance with the sample.

### 3) GENERAL THEORY

One very important material parameter in the study of thermoelectricity is the relaxation time of electrons in a material. This can be defined as:

$$\tau = \frac{\mu \cdot m^*}{q} \quad (3.1)$$

Where  $\tau$  is the average relaxation time of electrons,  $m^*$  is their effective mass, and  $\mu$  is the average mobility. The effective mass is the mass that a particle, whether hole or electron, appears to carry in the transport model in a crystal. The mobility is controlled by the scattering of carriers on imperfections, such as acoustical vibrations of the lattice, ionized, neutral, and magnetic impurities. Further, in simple cases, the relaxation time can be expressed as a power function in terms of temperature, effective mass, and carrier energy:<sup>(2)</sup>

$$\tau \propto E^{\lambda-1/2} T^s m_c^{*t} \quad (3.2)$$

where  $E$  is the energy of the carriers,  $T$  is the temperature,  $m_c^*$  is the conductivity effective mass, and  $\lambda$  is the scattering parameter. For both the PbTe and Bi<sub>2</sub>Te<sub>3</sub> based systems studied here, the conductivity effective mass,  $m_c^*$ , is given by the formula:

$$\frac{1}{m_c^*} = \frac{1}{3} \left( \frac{1}{m_l^*} + \frac{2}{m_t^*} \right) \quad (3.3)$$

where  $m_l^*$  and  $m_t^*$  are the carrier effective masses in the longitudinal and transverse directions, respectively. This assumes symmetry in the transverse direction, which holds for PbTe and Bi<sub>2</sub>Te<sub>3</sub>. The three exponents in (3.2) ( $\lambda, s, t$ ) vary based upon scattering mechanisms. In the case of acoustical vibrations,  $\lambda=0$ ,  $s=-1$ ,  $t=-3/2$ . In this case, mobility will increase with decreasing temperature. Ionized impurity scattering yields  $\lambda=2$ ,  $s=0$ ,  $t=1/2$ . The temperature dependence is removed and the energy of the carriers will have more influence on mobility. For scattering on grain boundaries or other static impurities,  $\lambda=1/2$ ,  $s=0$ ,  $t=1/2$ . Materials will exhibit a combination of different types of electronic scattering, and the relaxation times sum as:

$$\tau^{-1} = \sum_i \tau_i^{-1} \quad (3.4)$$

where  $\tau_i$  is the relaxation time for the  $i^{\text{th}}$  scattering process. Different scattering processes will be more influential on carrier mobility in different temperature ranges, thus creating a temperature dependence on the scattering parameter. For example, acoustical vibrations will have a dominant influence the scattering parameter at lower temperatures due to the  $T^{-1}$  relation than ionized impurity scattering, thus forcing the effective scattering parameter  $\lambda$  down towards zero.

#### 4 Parameter Fits – Non-Degenerate Case

For the two material systems discussed in this thesis, we use band structure theory to determine transport properties from measured galvanomagnetic and thermomagnetic properties. In particular, we use the *method of four coefficients*, which takes resistivity,

Nernst, Seebeck, and Hall coefficients and calculates Fermi Energy, carrier density and mobility, scattering parameter and density of states effective masses.

In the case of parabolic bands, we can find constant energy spheres in k-space by solving the Schrödinger equation:

$$E = \frac{\hbar^2}{2m^*} (k_1^2 + k_2^2 + k_3^2) \quad (3.5)$$

We take  $m^*$  to be the effective mass of the electron,  $\hbar$  is the reduced Planck constant, and  $k_{1,2,3}$  are the wavevectors in the three dimensions x,y,z. With  $k = \frac{n\pi}{L}$  along each direction where n is number of allowable states for electrons and L is the size of the crystal unit cell:

$$E = \frac{\hbar^2 \pi^2}{2m^* L^2} (n_1^2 + n_2^2 + n_3^2) \quad (3.6)$$

We make the hypothesis that a constant energy sphere of radius R is given by:

$$R = \left( \frac{E}{E_0} \right)^{1/2} \quad (3.7)$$

to make these calculations more transparent where  $R^2 = (n_1^2 + n_2^2 + n_3^2)$  and

$$E_0 = \frac{\hbar^2 \pi^2}{2m^* L^2}$$

The number of energy levels,  $N$ , inside the positive quadrant of the constant energy

surface sphere is  $N = \frac{1}{8} \frac{4\pi R^3}{3}$ . After normalizing for unit volume, the density of states

in this space is the derivative with respect to energy:

$$g(E) = \frac{dN}{dE} = \frac{\pi}{6} \left( \frac{E}{E_0} \right)^{3/2} = \frac{(2m^*)^{3/2}}{4\hbar^3 \pi^2} E^{1/2} \quad (3.8)$$

This function is seen in Figure 6 as the dotted curve. If, there is nonparabolicity of the bands, as in  $\text{Bi}_2\text{Te}_3$  and  $\text{PbTe}$ , we must make a correction to the energy dispersion relation of (3.5):

$$\gamma(E) = E \left( 1 + \frac{E}{E_g} \right) = \frac{\hbar^2}{2} \left( \frac{k_l^2}{m_l^*} + \frac{2k_t^2}{m_t^*} \right), \quad (3.9)$$

where  $E_g$  is the direct energy gap of the material and  $k$  and  $m^*$  are the wavevector and effective mass at  $k=0$  along the longitudinal and traverse directions. Note that the two transverse wave vectors that are normal to the longitudinal direction are equal in magnitude. The surface of constant energy is thus not a sphere (as in 3.7), but an ellipsoid of revolution. Following similar treatment as above, we obtain for the density of states:

$$g(E) = \frac{\sqrt{2}m_d^{*3/2}}{\pi^2 \hbar^3} \left( 1 + \frac{2E}{E_g} \right) \cdot \left( E + \frac{E^2}{E_g} \right)^{1/2} = \frac{\sqrt{2}m_d^{*3/2}}{\pi^2 \hbar^3} \gamma'(E) \sqrt{\gamma(E)} \quad (3.10)$$

Here  $\gamma'$  is the derivative of  $\gamma$  with respect to  $E$  and

$$m_d^* = \beta^{2/3} (m_l \cdot m_t^2)^{1/3} \quad (3.11)$$



is the density of states effective mass. The degeneracy number  $\beta$  is included for cases when the Fermi surface contains more than one pocket and  $\beta=4$  for PbTe and  $\beta=3$  for Bi<sub>2</sub>Te<sub>3</sub>. Subsequently, for nonparabolic bands, the energy dependence of relaxation time  $\tau$  is given by

$$\tau_e = \tau_0 \frac{\gamma(E)^{\lambda-1/2}}{\gamma'(E)}. \quad (3.12)$$

This indicates that the relaxation time is directly dependent on the carrier energy  $E$  multiplied by a prefactor. Carrier density is:

$$n = \int_0^{E_{\max}} g(E) f_0(E) dE, \quad (3.13)$$

where  $g(E)$  is the density of states given earlier and  $f(E)$  is the Fermi-Dirac distribution function. Substitution yields:

$$n = \frac{(2m_d^* k_B T)^{3/2}}{3\pi^2 \hbar^3} \int_0^{\infty} \gamma(z)^{3/2} \left( -\frac{\partial f_0}{\partial z} \right) dz, \quad (3.14)$$

$z=E/(k_B T)$  is the reduced energy where  $z$  is substituted in  $\gamma(E)$ . The electrical conductivity is given by:

$$\sigma_x = \int_0^{\infty} \frac{q^2 \tau}{m_d^*} \frac{df(E)}{dv_x} g(E) dE. \quad (3.15)$$

Manipulation of this formula yields:

$$\sigma = \frac{(2m_d^* k_B T)^{3/2}}{3\pi^2 \hbar^3} \frac{q^2}{m_c^*} \int_0^{\infty} \frac{\gamma(z)^{3/2}}{\gamma'(z)} \tau(z) \left( -\frac{\partial f_0}{\partial z} \right) dz \quad (3.16)$$

where  $m_c^*$  is the conductivity effective mass, as given by (3.3) It is the mass along the crystallographic direction along the applied field electric field or temperature gradient.

The introduction of a magnetic field for measurement of Hall and Nernst coefficients leads to increasingly complex formulas and derivations; therefore, only the final expressions will be written here. Next, we address the well known equation  $R_H = \frac{A}{n \cdot q}$ .

Coefficient  $A$  is close to unity if several conditions hold: single carrier conduction, the constant-energy surfaces are spherical, the energy dependence on crystal momentum is quadratic, and a relaxation time that is independent of energy. While these 4-parameter fits will not work in the regions of two carrier conduction, the other conditions can be taken into account in  $A$  and are incorporated into the following expression for low field ( $\mu B \ll 1$ ) Hall coefficient:

$$R_H = A \frac{1}{nq} \left( \frac{\int_0^\infty \frac{\gamma(z)^{3/2}}{(\gamma'(z))^2} \tau^2(z) \left( -\frac{\partial f_0}{\partial z} \right) dz \int_0^\infty \gamma(z)^{3/2} \left( -\frac{\partial f_0}{\partial z} \right) dz}{\left( \int_0^\infty \frac{\gamma(z)^{3/2}}{\gamma'(z)} \tau(z) \left( -\frac{\partial f_0}{\partial z} \right) dz \right)^2} \right) \quad (3.17)$$

where

$$A = \frac{3K(K+2)k_B}{(2K+1)^2}.$$

and  $K$  is the effective mass anisotropy coefficient  $K = m_l / m_t$  and corrects for a many ellipsoidal model. The low field isothermal Nernst coefficient is:

$$N = R_H \sigma \frac{k_B}{q} \left( \frac{\int_0^\infty \frac{\gamma(z)^{3/2}}{(\gamma'(z))^2} z \tau^2(z) \left( -\frac{\partial f_0}{\partial z} \right) dz}{\int_0^\infty \frac{\gamma(z)^{3/2}}{(\gamma'(z))^2} \tau^2(z) \left( -\frac{\partial f_0}{\partial z} \right) dz} - \frac{\int_0^\infty \frac{\gamma(z)^{3/2}}{\gamma'(z)} z \tau(z) \left( -\frac{\partial f_0}{\partial z} \right) dz}{\int_0^\infty \frac{\gamma(z)^{3/2}}{\gamma'(z)} \tau(z) \left( -\frac{\partial f_0}{\partial z} \right) dz} \right) \quad (3.18)$$

and the Seebeck coefficient is

$$S = \frac{k_B}{q} \left( \frac{\int_0^\infty \frac{\gamma(z)^{3/2}}{\gamma'(z)} z \tau(z) \left( -\frac{\partial f_0}{\partial z} \right) dz}{\int_0^\infty \frac{\gamma(z)^{3/2}}{\gamma'(z)} \tau(z) \left( -\frac{\partial f_0}{\partial z} \right) dz} - \frac{E_F}{k_B T} \right) \quad (3.19)$$

It follows that four independent parameters can be determined from the four measurements: (1) carrier mobility  $\mu$ , which includes  $\tau_0$  and  $m_c^*$ , (2) scattering parameter  $\lambda$ , (3) Fermi energy and (4) carrier density  $n$ . A fifth relevant parameter, the density of states effective mass  $m_d^*$ , is calculated from the carrier density and Fermi energy using a Kolodziejczak integral, which are of the form:

$${}_n \mathfrak{I}_k^m(E_f, T) = \int_0^\infty z^n (\gamma(z))^m \cdot (\gamma'(z))^k \left( \frac{df_0}{dz} \right) dz \quad (3.20)$$

and the density of states effective mass is then:

$$m_d^* = \left[ \frac{3\pi^2 \hbar^3}{(2k_B T)^{3/2}} \left( \frac{n}{{}_0 \mathfrak{I}_0^{3/2}(E_f, T)} \right) \right]^{2/3} \quad (3.21)$$

#### 4 Parameter Fits – Degenerate Case

The formula derived in the previous section is applicable to the non-degenerate case for semiconductors. This yields a computationally slow process as these need to be solved numerically. When the Fermi level lies deep in the band and the material is heavily

doped, the degenerate equations can be used instead of the non-degenerate equations. The Fermi function becomes  $f(E)=0$  for  $E>E_F$ , and  $f(E)=1$  for  $E \leq E_F$ . The equations are:

$$n = \frac{(2m_d^* \gamma(E))^{3/2}}{3\pi^2 \hbar^3} \quad (3.22)$$

$$\sigma = n \cdot q \cdot \mu(E_F) \quad (3.23)$$

$$R_H = \frac{3K(K+2)}{(2K+1)^2} \frac{1}{nq}, \quad (3.24)$$

$$S = \frac{\pi^2}{3} \frac{k_B}{q} k_B T \left[ \left( \lambda + \frac{3}{2} \right) \frac{\gamma'(E_F)}{\gamma'(E_F)} - 2 \frac{\gamma''(E_F)}{\gamma''(E_F)} \right], \quad (3.25)$$

$$N = R_H \sigma \frac{\pi^2}{3} \frac{k_B}{q} k_B T \left[ \lambda \frac{\gamma'(E_F)}{\gamma'(E_F)} - 2 \frac{\gamma''(E_F)}{\gamma''(E_F)} \right]. \quad (3.26)$$

These degenerate equations result in the same fits of the full equations as long as the Fermi energy is large enough and the material is degenerately doped.

### Electronic Two Carrier Fits

In this section, the nomenclature for electrical resistivity  $\rho_{xx}(B_z)$  and Hall resistance  $\rho_{xy}(B_z)$  is adjusted to be the diagonal and off-diagonal elements of the conductivity elements in a magnetic field  $B_z$  as  $\sigma_{xx}(B_z)$  and  $\sigma_{xy}(B_z)$ , respectively. This leads to:

$$\rho_{xx} = \frac{\sigma_{xx}}{\sigma_{xx}^2 + \sigma_{xy}^2} \text{ and } \rho_{xy} = \frac{\sigma_{xy}}{\sigma_{xx}^2 + \sigma_{xy}^2}. \quad (3.27)$$

With two carrier conduction, these equations expand to:

$$\rho_{xx}^{-1} = \frac{n \cdot q \cdot \mu_e}{1 + \mu_e^2 B_z^2} + \frac{p \cdot q \cdot \mu_h}{1 + \mu_h^2 B_z^2}, \quad \rho_{xy}^{-1} = \frac{n \cdot q \cdot \mu_e^2 B_z}{1 + \mu_e^2 B_z^2} + \frac{p \cdot q \cdot \mu_h^2 B_z}{1 + \mu_h^2 B_z^2} \quad (3.28)$$

where  $n, p$  are the electron and hole concentrations and  $\mu_e, \mu_h$  are the electron and hole mobilities. Note  $n$  and  $\mu_e$  have negative signs. Recalling that the low field Hall coefficient,  $R_H$ , is defined as the low field slope of  $\rho_{xy}(B_z)$ :

$$R_H = \lim_{B \rightarrow 0} \frac{d\rho_{xy}}{dB_z}. \quad (3.29)$$

Additionally, the magnetoresistance is expressed as (1.9).

We can perform Taylor series expansions around  $B=0$  for magnetoresistance and Hall coefficient as a function of magnetic field knowing that magnetoresistance is an even function and Hall is odd. Fitting these at each temperature as a function of field yields  $n, p, \mu_e, \mu_h$ , and therefore the partial hole and electron conductivities at zero field:

$$\sigma_e = nq\mu_e, \quad \sigma_h = pq\mu_h \quad (3.30)$$

with total conductivity as:

$$\sigma = \sigma_h + \sigma_e \quad (3.31)$$

and, in the limit for  $B_z \rightarrow 0$ :

$$R_H = \frac{1}{(p - n)q} \quad (3.32)$$

### Ambipolar Thermal Conductivity and the Wiedemann-Franz Law

The presence of both holes and electrons in a solid leads to the rise of ambipolar thermal conductivity. Refer to Figure 10 for a schematic of ambipolar thermal conductivity. This term is in addition to the heat that the electrons (or holes) carry across the material. Each carrier has an opposite Seebeck coefficient and electrical fluxes  $j(h^+)$  and  $j(e^-)$ , which are of opposite direction relative to the temperature gradient. Due to these opposing electrical fluxes and Seebeck coefficients both holes and electrons develop Peltier heat fluxes which are additive:

$$\Pi(e^-) = +(-S_e)j_e \quad \Pi(h^+) = -(+S_h)j_h \quad (3.33)$$

These act as an additional heat transfer mechanism with ambipolar thermal conductivity given as:

$$\kappa_{AMBI} = T \frac{\sigma_e \sigma_h}{\sigma_e + \sigma_h} (S_h - S_e)^2 \quad (3.34)$$

Where  $S_e$  and  $S_h$  are the partial Seebeck coefficients of the electrons and holes, respectively. No additional electrical flux through the material occurs as the Peltier heats are in parallel and the electrical fluxes are in series. The total thermal conductivity is now:

$$\kappa = \kappa_L + \sigma_e L_e T + \sigma_h L_h T + \kappa_{ambi} \quad (3.35)$$

where  $L_e$  and  $L_h$  are the electron and hole Lorenz numbers, as is discussed subsequently.

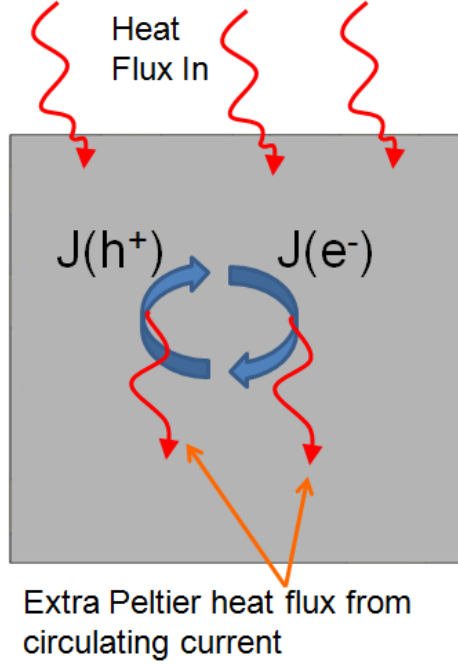


Figure 10: Schematic of ambipolar conductivity. The circulating electron and hole fluxes create an extra Peltier heat flux yet no net additional electrical current.

The Wiedemann-Franz law relates the electronic portion of thermal conductivity to the electrical conductivity of a material, assuming single carrier conduction, through the relation:

$$\kappa_e = \sigma \cdot L \cdot T \quad (3.36)$$

We note the importance of this relation as one can calculate  $\kappa_L$  using (3.35) with single carrier conduction by subtracting electronic thermal conductivity from the measured total thermal conductivity. The Lorenz number must be calculated as it is a function of temperature, Fermi level, and scattering exponent. Using Kolodziejczak integrals (3.20), the Lorenz number can be expressed as:

$$L = \left( \frac{k_b}{q} \right)^2 \left[ \left( \frac{{}^2\mathfrak{I}_{-2}^{\lambda+1}(E_f, T)}{{}^0\mathfrak{I}_{-2}^{\lambda+1}(E_f, T)} - \frac{{}^1\mathfrak{I}_{-2}^{\lambda+1}(E_f, T)}{{}^0\mathfrak{I}_{-2}^{\lambda+1}(E_f, T)} \right)^2 \right] \quad (3.37)$$

### Shubnikov-de Haas Oscillations and the Fermi Surface

The Shubnikov-de Haas (SdH) effect describes an oscillation in the electrical resistivity of a single crystal that occurs at high magnetic fields and low temperatures as first witnessed by L. Shubnikov and W.J. Haas.<sup>(18)</sup> When these conditions are met ( $\mu B > 1$ ), the free electrons, or holes, in the conduction (valence) band of a conducting material, behave as simple harmonic oscillators with a frequency, termed the cyclotron frequency, that is inversely proportional to the applied magnetic field ( $H^{-1}$ ).<sup>(19)</sup> This effect allows for a direct measurement of the Fermi surface of a material.

To show that this correlation between Fermi surface and the SdH effect is correct we must start with Brillouin zones and the reciprocal lattice. The Brillouin zone is defined as the first primitive cell in the reciprocal lattice in the frequency domain. The periodic lattice leads to the effect of carving the energy distribution for conduction electrons into a series of bands. This occurs because the allowed wave vector states in a 3D lattice as defined in the Brillouin zone are not located in the same spot, thus creating an intertwined allowed wave vector region. We define wavenumber  $k$  by the relation  $p = \hbar \cdot k$  where  $p$  is the momentum of an electron and  $\hbar$  is the reduced Plank constant. Next, the acceleration of a wave-packet experiencing force  $F$  is  $\hbar \cdot \dot{k} = F$ . With an applied magnetic field, the Lorenz force is  $\hbar \cdot \dot{k} = q \cdot v(k) \times H$  where  $v(k) = \frac{1}{\hbar} \cdot \nabla_k E(k)$ . Reference



Figure 11 for a schematic. We see that velocity of an electron in the state  $k$  is the local gradient of the state of energy  $E(k)$ . Taking the derivative of  $v(k)$ :

$$\dot{v}(k) = \frac{\partial}{\partial t} \left( \frac{1}{\hbar} \cdot \nabla_k E(k) \right) = \frac{\partial k}{\partial t} \frac{\partial}{\partial k} \left( \frac{1}{\hbar} \cdot \frac{\partial E(k)}{\partial k} \right) = \frac{qE}{\hbar} \left( \frac{1}{\hbar} \cdot \frac{\partial^2 E(k)}{\partial k^2} \right) = \frac{qE}{\hbar^2} \left( \frac{\partial^2 E(k)}{\partial k^2} \right). \quad (3.37)$$

Where  $E$  is the electric field and  $E(k)$  is the energy dispersion relation. Further,

$$\frac{\dot{v}}{qE} = \frac{1}{\hbar^2} \left( \frac{\partial^2 E(k)}{\partial k^2} \right) = \frac{1}{m^*} \quad (3.38)$$

where  $m^*$  is defined as the electron's effective mass. We see here that the effective mass is inversely proportional to the second derivative of the energy dispersion relation with respect to the wave-vector.

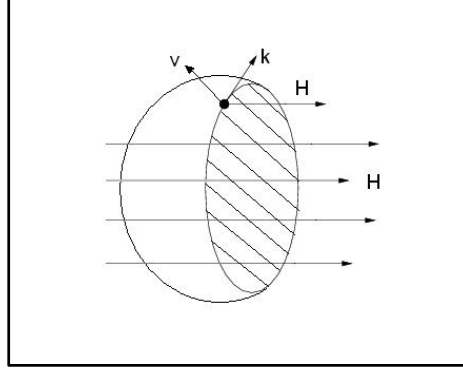


Figure 11: Fermi surface of a constant energy sphere. The magnetic orbit (shaded section) is the intersection of the Fermi surface with a plane normal to the magnetic field. The location of the intersection of the magnetic field and the Fermi surface changes as the magnetic field varies.

This leads to the derivation of cyclotron frequency. With the vector state  $k$  altered by a

magnetic field:  $\dot{k} = \frac{q}{\hbar} v \times H$ , the motion of the point in  $k$ -space is normal to the magnetic

field and stays on the same plane in k-space as in Figure 11. This motion is normal to the electron velocity  $\mathbf{v}$  and thereby is normal to the constant energy surfaces in k-space.  $\dot{\mathbf{k}}$  must then lie in the plane tangent to  $E(\mathbf{k})$ . In Figure 11, we show a Fermi surface represented as a sphere for simplicity. The k-vector of an electron traces out the orbit created by the intersection of the Fermi surface with a plane normal to  $\mathbf{H}$  (shown as the cut out of the sphere). A magnetic field does not change the energy of an electron, it merely deflects it into a helicoidal path in real space. In vector space this is easy to define as an orbit. The chosen point will complete one orbit in time  $T$ :

$$T = \frac{2\pi}{\omega_H} = \frac{\hbar}{qH} \oint \frac{d\mathbf{k}}{v_{\perp}} \quad (3.39)$$

where  $v_{\perp}$  is the velocity normal to  $\mathbf{H}$ .  $\omega_H$  is known as the cyclotron frequency and for a free electron sphere is given by:

$$\omega_H = \frac{qH}{m} \quad (3.40)$$

For a spherical Fermi surface, the frequency will be the same for magnetic fields applied in different directions; this is not true for Fermi surfaces of varying shape. We use the fact that we can quantize the energy of any system that is periodic with time in units of  $\hbar\omega_H$  to write  $E_n = (n + \phi)\hbar\omega_H$ , where  $\phi$  is a phase angle and  $n=1,2,3$ . Rewriting (3.40), we obtain:

$$\omega_H = \frac{2\pi \cdot q \cdot H}{\hbar} \left[ \oint \frac{d\mathbf{k}}{v_{\perp}} \right]^{-1}. \quad (3.41)$$

Recalling that  $v$  is proportional to the gradient of  $E(k)$ , a small change in energy,  $\Delta E$ , moves a distance  $\Delta k_{\perp} = \frac{\Delta E}{\hbar v_{\perp}}$  in  $k$ -space, as depicted in Figure 12. This leads to a new energy orbit  $E + \Delta E$ . The previous integral is then proportional to  $\Delta A$ , which is the area in the  $k$ -plane between the two orbits. Further,

$$\Delta A_F = \frac{2\pi \cdot q \cdot H}{\hbar^2} \frac{\Delta E}{\omega_H} \quad (3.42)$$

which gives for the cyclotron frequency:

$$\omega_H = \frac{2\pi \cdot q \cdot H}{\hbar^2} \left( \frac{\partial E}{\partial A_F} \right) \quad (3.43)$$

The earlier assertion that the energy is quantized indicates that the area of the orbit is

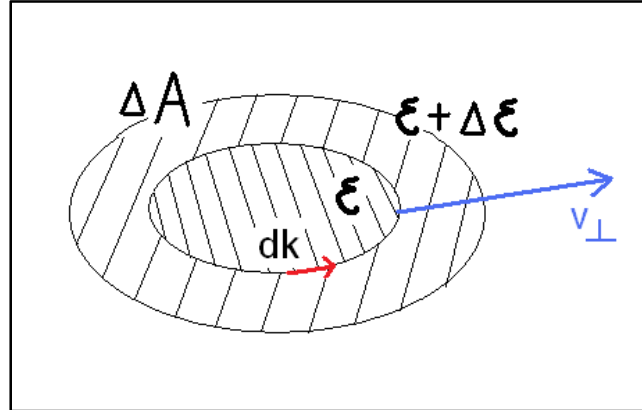


Figure 12: Geometry of quantization of orbits. With a small change in energy  $\Delta E$ , a distance  $\Delta k$  is moved in  $k$ -space. The integral around the new ellipse in  $k$ -space is proportional to  $\Delta A$ . This allows for the relation between the cyclotron frequency and  $\Delta E/\Delta A$ .

quantized in units of  $\frac{2\pi \cdot q \cdot H}{\hbar}$  and therefore, for the total area of orbit  $E_n$ :

$$A_F = (n + \phi) \cdot \frac{2\pi \cdot q \cdot H}{\hbar} \quad (3.44)$$

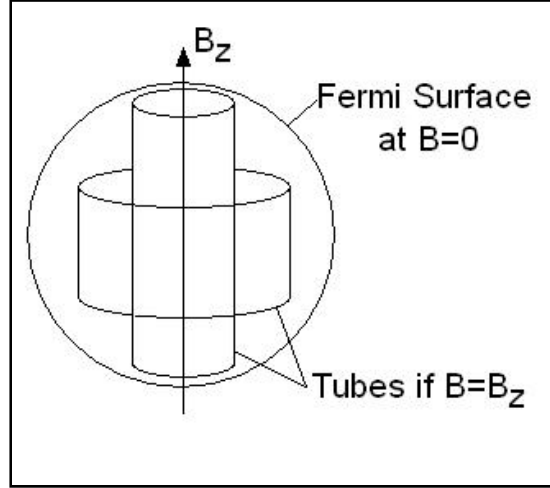


Figure 13: At zero field, the Fermi surface is a sphere. However, a magnetic field forces a re-quantization of the Fermi surface into 'tubes' of varying energies.

This development indicates that the magnetic field 're-quantizes' the electron gas in the normal directions. The application of a magnetic field divides k-space into 'tubes' of constant cross sectional area each corresponding to the states of constant magnetic quantum number as depicted in Figure 13. This is changed from the previous distribution of  $E(k)$  where it was a function of  $k$  with points uniformly distributed in k-space. Each state is forced to change its energy up or down a small amount in order to concentrate onto the surface of the nearest allowed quantum state. At normal temperatures and low fields, this does not make an impact on the overall energy, as those states that move up are compensated by those that move down. However, when considering a sharp Fermi surface in a pure single crystal, it is possible to witness this effect. As the magnetic field

is increased, the tubes move outward, because the area of each is proportional to  $H$ . Eventually, and repeatedly, a tube will sweep by the Fermi surface at a cross section of maximum area. This is shown in Figure 14 . As one tube crosses the energy level, the energy of the states in the region is increased as these levels attempt to condense as shown in (14a). Then, as the next tube approaches the Fermi level, more states become available because the size of the tube's area is proportional to  $H$  as in (14b). This leads to the decrease in energy to that below the average value. This leads to an oscillation in the energy of the electron gas that is periodic in the magnetic field quantum number, i.e.

$\frac{2\pi \cdot q \cdot H}{\hbar}$ . One can then express the period of oscillation in terms of the magnetic field

as:

$$\Delta \frac{1}{H} = \frac{2\pi \cdot q}{\hbar A_F}. \quad (3.45)$$

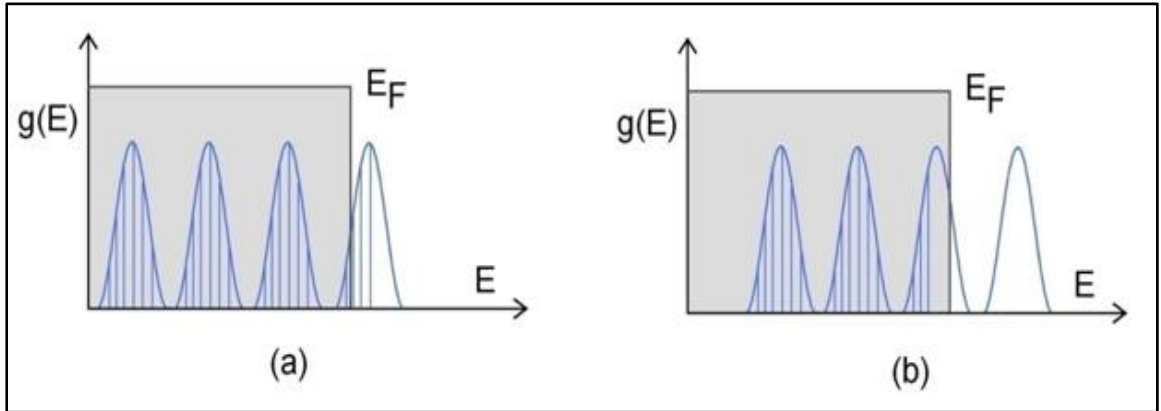


Figure 14: Schematic of the magnetic field quantized density of states in the direction perpendicular to the field. As the field is increased, the available states increase in energy and pass through the Fermi level. This creates the oscillations that appear in  $1/\text{magnetic field}$ .

As the number of available conduction electrons (or holes) will vary with the oscillations of available energy states right around the Fermi level, the electrical resistivity will oscillate with same frequency that the tubes cross the Fermi Level and thus yields the area of the Fermi surface normal to direction of the applied magnetic field.

## 4) LEAD TELLURIDE LEAD SULFIDE

### Introduction

Lead telluride has been the standard thermoelectric material used in the temperature range 200-500 °C since the early 1950's. However, the highest  $zT$  in p-type material has traditionally been limited to approximately 0.7 at 500 °C and to 1 in n-type material. In this work, an attempt is made to increase the  $zT$  of PbTe based material through the precipitation of nanoscale PbS morphology in a bulk PbTe matrix. Both PbTe and PbS form NaCl-type lattices of the  $m3m$  symmetry class. X-ray diffraction shows that the lattice constant for PbTe is 6.50 Angstroms and 5.94 Å for PbS.<sup>(2)</sup> The unit cell is face-centered cubic and all atoms have a coordination number of 6. Both are highly brittle and have a tendency to cleave along the (100) planes. The chemical binding is described as mixed ionic-covalent and can be classified as polar semiconductors. Lead telluride is a narrow gap semiconductor with a direct energy gap of 0.32 eV at 300K; lead sulfide has a gap of 0.41 eV. Its Fermi surfaces can be described by a four ellipsoidal model, where the ellipsoids lie in the  $\langle 111 \rangle$  direction (L-point). Its effective mass ellipsoids have two different effective masses, corresponding to the one longitudinal and two transverse directions.<sup>(20)</sup>

For this thesis, bulk samples of  $(\text{Pb}_{1-x}\text{Sn}_x\text{Te})_{1-y}(\text{PbS})_y$  have been prepared with  $y$  in the range 4% to 30% and  $x=5\%$  at Northwestern University under the direction of Professor M. Kanatzidis, and a set of  $(\text{PbTe})_{1-y}(\text{PbS})_y$  samples were prepared at OSU. For

simplicity, the  $\text{Pb}_{95}\text{Sn}_5\text{Te}$  portion will be referred to henceforth as PbTe. There is a miscibility gap in the pseudo-binary PbTe/PbS phase diagram that enables the precipitation of a PbS-rich phase in a PbTe-rich matrix, as seen in Figure 15. To that effect, the samples were compounded in the liquidus, and then quenched, forming a supersaturated solution. The goal of this study was the development of an optimal precipitation annealing schedule. Samples with nano-precipitates of a PbS-rich phase in a PbTe-rich parent phase have been obtained, as evidenced by X-ray diffractions. This technique, previously applied to Pb-rich PbTe<sup>(21)</sup>, is aimed at creating a bulk material containing a substantial fraction of nanometer-sized particles in order to mimic the morphology of quantum-dot superlattices. By introducing nanoparticles, we expect a reduction in  $\kappa_L$  and an increase of the thermoelectric figure of merit. Galvanomagnetic and thermomagnetic properties were measured and the calculated electrical properties of the materials are discussed.

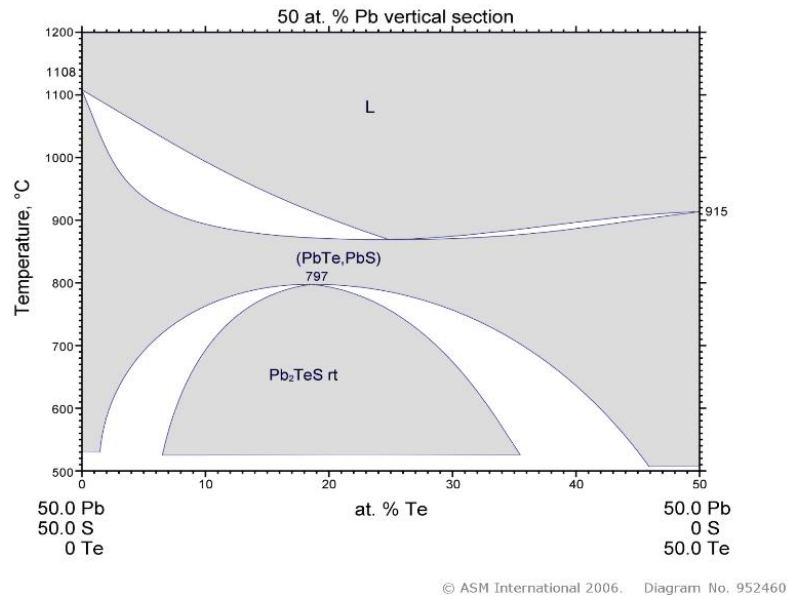


Figure 15: Phase diagram for the PbTe-PbS system. Pure PbS is on the left; PbTe the right. It is in the miscibility gap (non shaded region) that PbS rich regions are precipitated out of the PbTe matrix. As the anneal is at 500 °C, the matrix has the approximate composition  $\text{PbTe}_{95}\text{S}_5$ .<sup>(22)</sup>



The samples were sealed under high vacuum in quartz ampoules and heated to 1000 C. After cooling through the liquidus, the materials were kept at 773K for 72hr. This anneal allows for the precipitation of nanoscale PbS rich regions in a PbTe rich matrix. Transmission electron microscopy imaging showed spinodal decomposition and nucleation and growth.<sup>(11)</sup> The 30% PbS sample showed mainly spinodal decomposition; the 4% nucleation and growth. The 8% and 16% samples have combinations of both. In fact, microscopy shows spinodal decomposition dominated regions and nucleation and growth dominated regions on the same sample. They contain alternating segments of each. Besides the samples received from the Northwestern University group, several samples of PbTe-PbS were made in-house following similar heat treatment schedules for microscopy imaging. Figure 16 is a SEM image showing nanoscale PbS inclusions in a PbTe matrix. The samples were not optimally doped, and therefore not electrically characterized here.

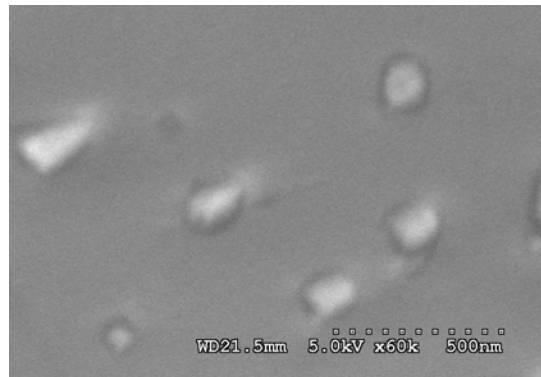


Figure 16: SEM image of PbTe-PbS showing nanoinclusions of PbS prepared at OSU. It is believed that these inclusions scatter phonons and not electrons, thus decreasing thermal conductivity without adversely affecting electrical resistivity. The PbS dots are 30-50 nm in diameter.

## Measurements and Discussion

The materials underwent galvanomagnetic and thermomagnetic measurements described in Section 2. A conventional flow cryostat was used in the range 80-580 K and -1.5 to 1.5 Tesla. Refer to Figure 17 for the measured electrical properties of this material. Electrical resistivity for the  $4\% < y < 16\%$  samples is very close, within ten percent while the 30% sample exhibits an increased resistivity. This indicates that the PbS content of the 30% sample has reached too high a value and thus begins to scatter electrons on the nanoscale morphology. Further, the 8% and 16% samples have a resistance that continuously decreases with temperature, thereby showing a more metallic character. A similar trend holds for the thermopower, with the 30% having the lowest value and the 4% and 8% the highest. The Seebeck coefficient behavior appears to be more related to carrier density than PbS content. The 8% sample has the best thermoelectric power factor. We see a small Hall coefficient, which reflects the materials high doping level – on the order of  $10^{19} \text{ cm}^{-3}$  carriers. The Nernst coefficient is high, reflecting a large scattering coefficient, which is due to the presence of a second phase PbS in the bulk matrix PbTe.

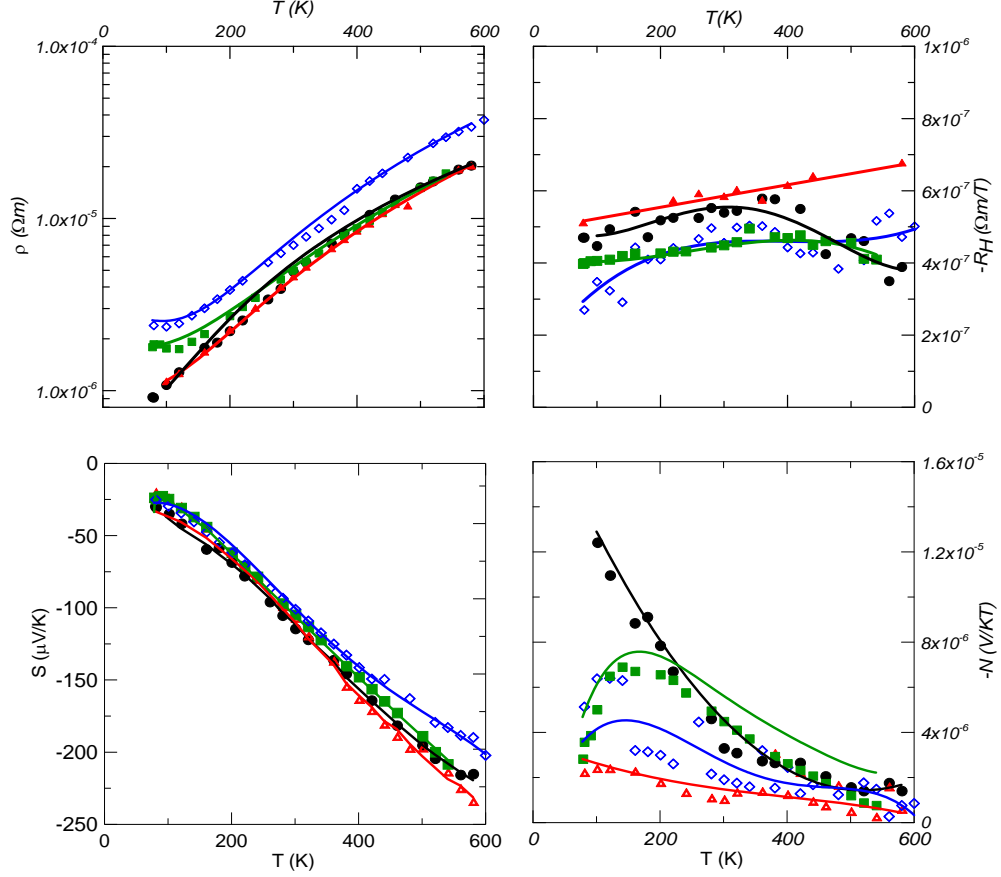


Figure 17: Galvanomagnetic (resistivity  $\rho$  and Hall coefficient  $R_H$ ) and thermomagnetic (Seebeck  $S$  and isothermal transverse Nernst  $N$  coefficients) data as a function of temperature for the samples studied. The points indicate the measured data, while the lines represent the recalculated properties using the calculated values for Fermi Energy, carrier density, effective mass, and scattering parameter. The symbols are: (●)  $(\text{PbTe})_{96}(\text{PbS})_4$ , (▲)  $(\text{PbTe})_{92}(\text{PbS})_8$ , (■)  $(\text{PbTe})_{84}(\text{PbS})_{16}$ , (◇)  $(\text{PbTe})_{70}(\text{PbS})_{30}$ .

The relation between Seebeck and carrier density for PbTe (carrier densities  $8 \times 10^{18}$  -  $4 \times 10^{19} \text{ cm}^{-3}$ ) is plotted in Figure 18. This relation has been named after Pisarenko, who proposed a relation to calculate the general dependence of Seebeck coefficient as a function of carrier density for any semiconductor.<sup>(23)</sup> The Pisarenko relation is discussed further in Section 5. In the case of PbTe, we calculate Seebeck coefficient for acoustic phonon scattering ( $\lambda=0$ ) and plot this as the solid line in Figure 18. This relation has been shown to generally hold true for all PbTe dopants such as iodine, sodium, antimony, etc.

We see here that the samples in this study fall underneath the line. This indicates that the PbS negatively affects thermopower by 10-20% compared to pure PbTe.

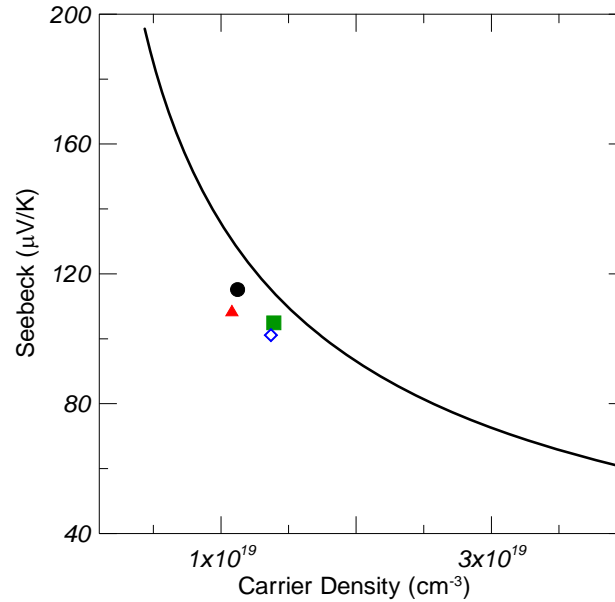


Figure 18: Seebeck coefficient against carrier density at 300K. The solid curve is the Pisarenko relation for bulk PbTe. We note that all samples in this series fall below the curve. The symbols are: (●)  $(\text{PbTe})_{96}(\text{PbS})_4$ , (▲)  $(\text{PbTe})_{92}(\text{PbS})_8$ , (■)  $(\text{PbTe})_{84}(\text{PbS})_{16}$ , (◆)  $(\text{PbTe})_{70}(\text{PbS})_{30}$ .

Figure 19 depicts the power factor and carrier densities for the materials as functions of temperature. The curve with plus symbols (+) shows the power factor of a lead telluride doped to a similar carrier density as the PbTe-PbS samples studied here. The 4% PbS sample has a power factor consistent with pure PbTe. There is an increase in  $P$  for the 8% PbS sample over that of the 4% but as the sulfur content is increased further the  $P$  begins to fall, with 16% slightly less than the 4% and the 30% less than half of the 4%. We see here that the aforementioned decrease in Seebeck compared to bulk PbTe is compensated by a corresponding decrease in electrical resistivity for the 4% and 8%. At higher PbS concentrations, the power factor is negatively impacted. The 8% sample has a higher

power factor at 300K than a similarly doped PbTe sample that is included for comparison. The carrier densities for the samples is close between  $1-2 \times 10^{19} \text{ cm}^{-3}$ , and does not vary significantly with temperature. These doping levels are optimized for operation as thermoelectric materials in temperatures between 250-450 °C.<sup>(2)</sup>

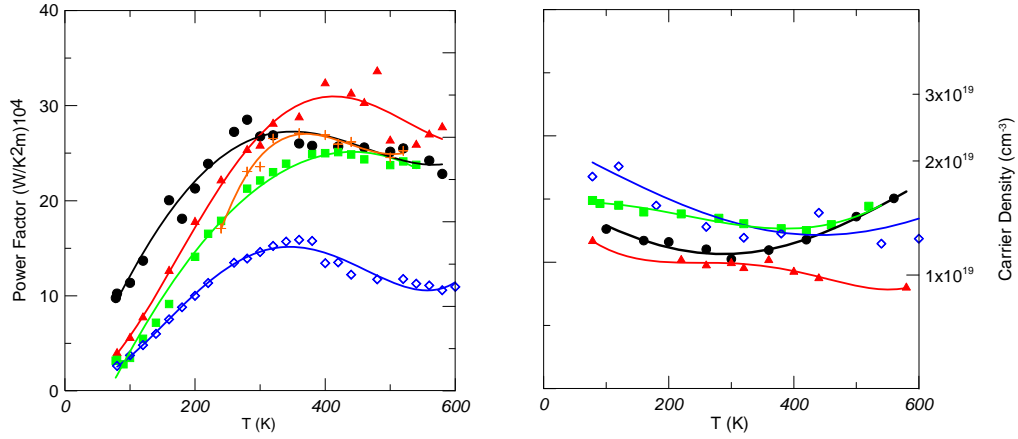


Figure 19: Power factor and carrier density as functions of temperature. A similarly doped PbTe is included in the power factor plot for comparison. The symbols are: (●) (PbTe)<sub>96</sub>(PbS)<sub>4</sub>, (▲) (PbTe)<sub>92</sub>(PbS)<sub>8</sub>, (■) (PbTe)<sub>84</sub>(PbS)<sub>16</sub>, (◆) (PbTe)<sub>70</sub>(PbS)<sub>30</sub>.

The four parameter fits that were introduced in Section 3 were performed on the experimental data for each sample. The results are shown in Figure 20. We see that the addition of PbS to PbTe results in a decrease in effective mass compared to Pb<sub>95</sub>Sn<sub>5</sub>Te for all of the alloys, with the 4% and 30% showing the greatest decrease. All exhibit a positive dependence on increasing temperature. This is to be expected because the conduction band of PbTe has a heavier mass at higher temperatures.<sup>(2)</sup> We see a decreasing Fermi level with increasing temperature due to the onset of intrinsic conduction with increasing temperature. There is a large increase in the scattering parameter over that of PbSnTe. There is no relation, however, between PbS content and scattering parameter. The mobility for the 8% sample is not reduced; the others are

reduced by up to a factor of 2. The high mobility and effective mass for the 8% sample indicates that the sample has the longest relaxation time.

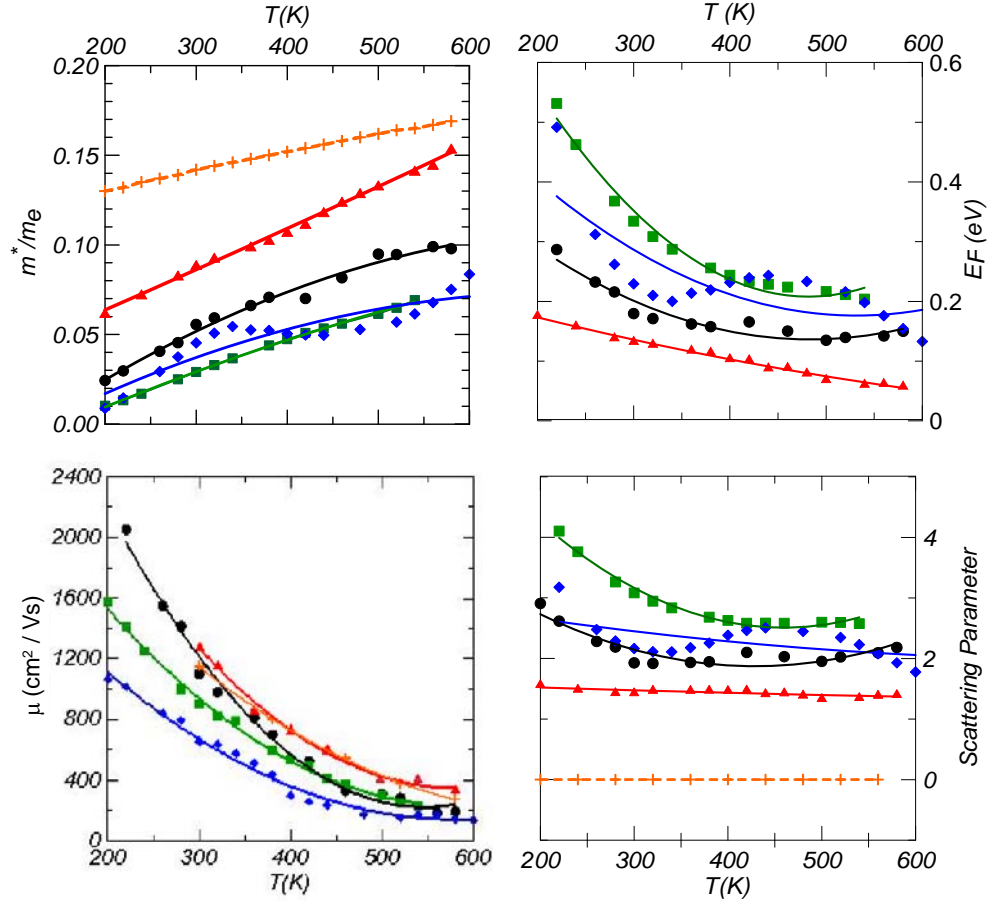


Figure 20: Summary of 4-parameter fit on the PbTe/PbS system. The symbols are: (●) (PbTe)<sub>96</sub>(PbS)<sub>4</sub>, (▲) (PbTe)<sub>92</sub>(PbS)<sub>8</sub>, (■) (PbTe)<sub>84</sub>(PbS)<sub>16</sub>, (◆) (PbTe)<sub>70</sub>(PbS)<sub>30</sub>. (+) Pb<sub>95</sub>Sn<sub>5</sub>Te. We note the decrease in effective mass of the PbTe-PbS system compared to standard PbSnTe. Additionally, the scattering parameter is greatly increased, ranging from 1.5-3.5 at 300K.

Table 3.1 contains a summary of 300 K properties of the studied alloys. The carrier densities are close to each other in all samples, indicating a constant doping level. Further, the mobilities, compensated for carrier density, decrease with increasing PbS content, except for the 8% sample. This behavior is also exhibited in the 300K electrical

resistivity values. We also see a decrease in Seebeck coefficient with increasing PbS content.

In conclusion, we note that the introduction of PbS to PbTe is successful at increasing  $zT$  because its reduction in thermal conductivity doesn't adversely affect electronic conductivity. There is no enhancement in thermopower in essence because the increase in scattering parameter  $\lambda$ , which by itself should increase  $S(n)$ , is compensated by the fact that the effective mass decreases with increasing concentration of PbS. Further, for the 8% sample, the decrease in thermopower is compensated by a greater increase in electrical conductivity, which is consistent with the fact that effective mass is decreased, and actually leads to an increase in power factor. It is not exactly clear why the 8% has the highest power factor and  $zT$ , however, it appears that this sample has reached an optimum between the two competing effects, increased scattering parameter but decreased effective mass.

Composition	n	$\mu$	$R_H$	$\rho$	S	P	N	$\lambda$	$m^*$
	(cm <sup>-3</sup> )	(cm <sup>2</sup> /Vs)	( $\mu\Omega$ m/T)	(m $\Omega$ cm)	( $\mu$ V/K)	(mW/mK <sup>2</sup> )	( $\mu$ V/TK)	(-)	(me)
PbSnTe									
								0	0.14
(Pb <sub>95</sub> Sn <sub>5</sub> Te) <sub>96</sub> (Pbs) <sub>4</sub>	1.16E+19	1102	0.54	0.49	-114	2.65	3.6	1.9	0.05
(Pb <sub>95</sub> Sn <sub>5</sub> Te) <sub>92</sub> (Pbs) <sub>8</sub>	1.08E+19	1289	0.58	0.45	-108	2.59	1.3	1.5	0.08
(Pb <sub>95</sub> Sn <sub>5</sub> Te) <sub>84</sub> (Pbs) <sub>16</sub>	1.40E+19	901	0.45	0.50	-105	2.22	5.4	3.1	0.03
(Pb <sub>95</sub> Sn <sub>5</sub> Te) <sub>70</sub> (Pbs) <sub>30</sub>	1.36E+19	657	0.46	0.70	-101	1.46	2.6	2.2	0.04

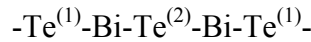
Table 1: Properties of PbSnTe-Pbs alloys studied at 300K. the carrier density  $n$  is given in column 2, then electrical mobility  $\mu$ , Hall coefficient  $R_H$ , resistivity  $\rho$ , Seebeck coefficient  $S$ , power factor ( $P=S^2\sigma$ ), Nernst coefficient  $N$ , scattering parameter  $\lambda$ , and density of states effective mass  $m^*$ .



## 5) BISMUTH TELLURIDE

### Introduction

Bismuth Telluride is the most commonly used semiconductor in TE applications near room temperature. Its maximum  $zT$  has historically been limited to approximately 1.  $\text{Bi}_2\text{Te}_3$  is typically alloyed with antimony and selenium as these increase both peak  $zT$  and the temperature of peak  $zT$ . It is an indirect gap semiconductor with a hexagonal unit cell that is formed by the stacking of layers perpendicular to the trigonal axis. The sequence that is formed is:



The superscripts refer to the type of bonding. These  $\text{Te}^{(1)}-\text{Te}^{(1)}$  bonds are considered to be Van der Waals bonding and are responsible for the easy cleavage of  $\text{Bi}_2\text{Te}_3$  along the trigonal axis. They also lead to an extremely low lattice thermal conductivity. It is this reason that polycrystalline material has to be used in thermoelectric devices. The  $\text{Bi}-\text{Te}^{(2)}$  and  $\text{Bi}-\text{Te}^{(1)}$  bonds are considered ionic-covalent, as in  $\text{PbTe}$ .<sup>(24)</sup> This system also exhibits anisotropy in its thermoelectric characteristics.

Before continuing, it is useful to outline the Brillouin zone and the notation used in discussing  $\text{Bi}_2\text{Te}_3$ . The symmetry operators of the  $\text{Bi}_2\text{Te}_3$  space group are: 1) one 3-fold rotation axis, 2) three reflection planes containing the 3-fold axis at  $120^\circ$  with each other, 3) three 2-fold rotation axis perpendicular to the 3-fold axis that lie halfway between the reflection planes, and 4) an inversion center. The Cartesian coordinate system that is

used has the z (3 or trigonal) axis parallel to the 3-fold rotation axis, the y (2 or bisectrix) axis in a reflection plane, and the x (1 or binary) axis along a 2-fold rotation axis.<sup>(25)</sup>

Refer to Figure 21 for a schematic of the Brillouin zone.

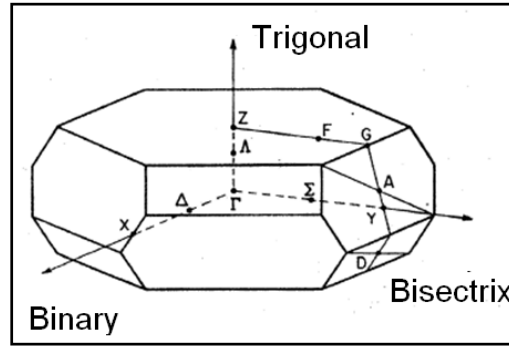


Figure 21: Brillouin zone for  $\text{Bi}_2\text{Te}_3$  containing the location of symmetry points.<sup>(26)</sup>

$\text{Bi}_2\text{Te}_3$ 's conduction and valence bands have six general ellipsoids, with each centered on a mirror plane of the Brillouin zone. The valence bands are centered in the mirror plane of the Brillouin zone and have their main axes in the mirror planes tilted by  $25^\circ$  relative to the crystal axes. There is conflicting data on the width of the band gap and bottom of the band effective masses; in this work we take  $E_g(0\text{K}) = 0.16\text{eV}$ ,  $E_g(300\text{K}) = 0.13\text{eV}$ ,<sup>(27)</sup> bottom of the conduction band density of states effective mass =  $0.081\text{ me}$ ,<sup>(28)</sup> and top of the valence band density of states effective mass =  $0.106\text{ me}$ .<sup>(29)</sup> A second, heavier valence band consisting of six ellipsoids is proposed to lay  $20.5\text{ meV}$  below the highest valence band at  $2\text{K}$ .<sup>(29)</sup> Similarly, a second conduction band lying  $30\text{ meV}$  above the lowest conduction band at  $2\text{K}$  is proposed.<sup>(30)</sup> Antistructural defects, where bismuth atoms occupy tellurium lattice positions, force the semiconductor naturally p-type. These defects in zone refined  $\text{Bi}_2\text{Te}_3$  lead to an excess of  $2 \times 10^{19}$  holes. This occurs whether the starting material contains excess tellurium or bismuth.<sup>(31)</sup>

### Pisarenko Relation for P-Type Bismuth Telluride

The relation, such as that suggested by Ravich for PbTe and  $\text{Pb}_{1-x}\text{Sn}_x\text{Te}$ , is known as the Pisarenko relation (see Figure 18).<sup>(2)</sup> This relationship is necessary in order to establish if one has successfully modified the density of states and increased Seebeck for a given carrier concentration and scattering mechanism. The Pisarenko expression for a generic one carrier semiconductor is:<sup>(23)</sup>

$$S = \frac{k}{\sigma} \left[ \mu \cdot n \cdot \left[ A(\lambda) + \ln \frac{2(2\pi m^* k_b T)^{3/2}}{h^3 n} \right] \right] \quad (5.1)$$

where  $\mu$  is the carrier mobility,  $n$  is the carrier density,  $m^*$  is the carrier effective mass, and  $A(\lambda)$  is a constant that depends on the scattering mechanism. When holes and electrons are present, (5.1) is generalized to:<sup>(23)</sup>

$$S = \frac{k}{\sigma} \left[ \mu \cdot n \cdot \left[ A(\lambda) + \ln \frac{2(2\pi m_e^* k_b T)^{3/2}}{h^3 n} \right] - \nu \cdot p \cdot \left[ A(\lambda) + \ln \frac{2(2\pi m_h^* k_b T)^{3/2}}{h^3 p} \right] \right] \quad (5.2)$$

where  $\mu$  and  $\nu$  are the electron and hole mobilities,  $n$  and  $p$ , are the carrier densities,  $m_e^*$  and  $m_h^*$  are the electron and hole effective masses. We note that if we have two hole or electron bands, instead of bipolar conduction, we can modify (5.2) to sum both bands' contributions to Seebeck, instead of subtracting, as carriers of the opposite sign do. We see that the Seebeck coefficient, in a system with two carrier conduction, is a relation between both holes and electrons, their mobilities, and the scattering mechanism. With constant effective mass, and for a single carrier system, the Seebeck coefficient is a logarithmically decaying function with increasing carrier density. While this relation is well established in the PbTe system (Figure 18), in our literature search we did not find it

for the  $\text{Bi}_2\text{Te}_3$  system. We therefore set out to calculate it as per Section 3 for p-type  $\text{Bi}_2\text{Te}_3$ . Refer to Figure 22 for a plot containing published data and our calculated 300K Pisarenko relation for  $\text{Bi}_2\text{Te}_3$  assuming  $\lambda=3/2$ , for ionized impurity scattering.

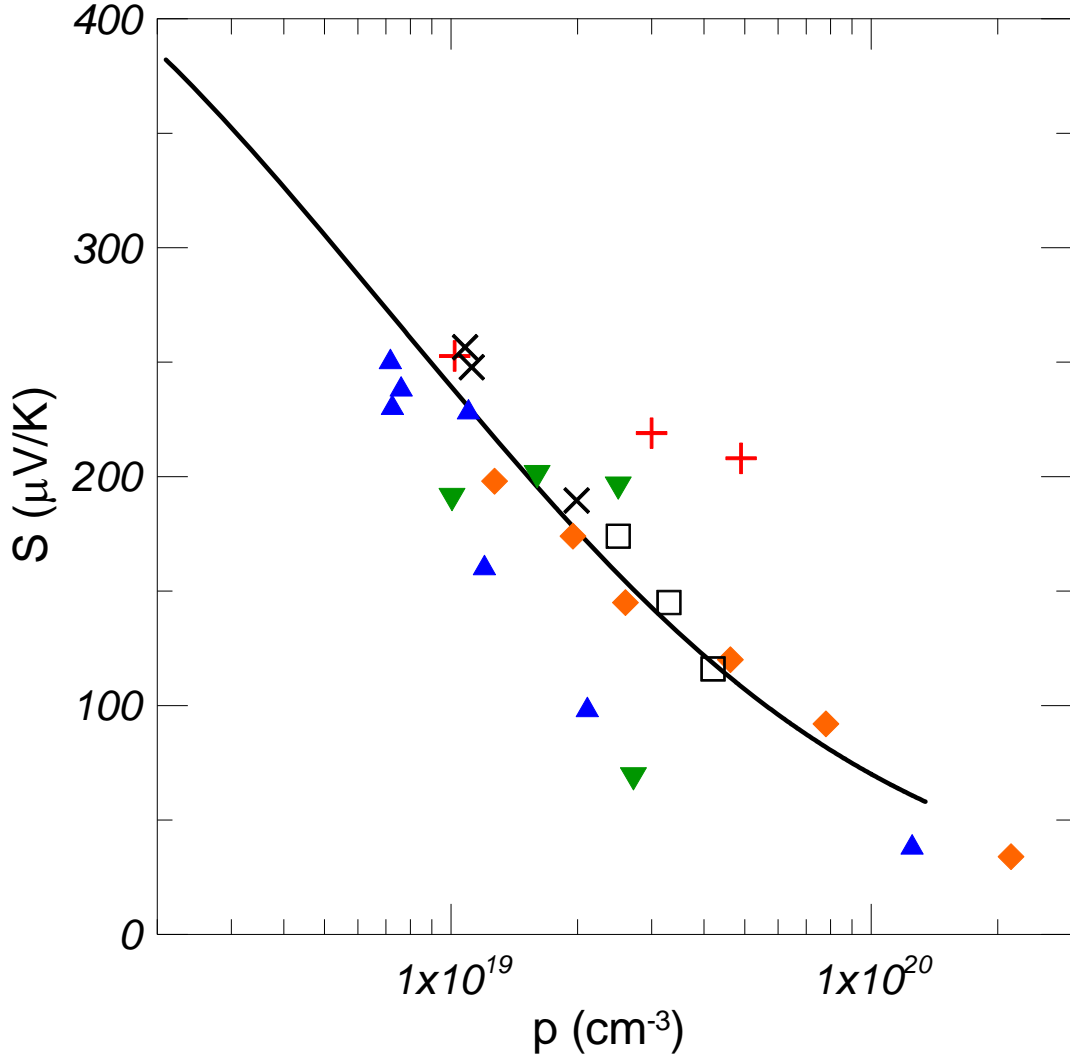


Figure 22: Pisarenko relation for p-type  $\text{Bi}_2\text{Te}_3$  as calculated at 300K. The solid line represents the calculation. The symbols are (+)  $\text{Bi}_2\text{Te}_3\text{:Sn}$  as reported in this thesis, (◆)  $\text{Bi}_2\text{Te}_3$  doped with Pb<sup>(32)</sup>, (▼)  $\text{Bi}_2\text{Te}_3\text{:Sn}$  with other Sn concentrations<sup>(33)</sup>, (▲)  $\text{Bi}_2\text{Te}_3$  doped with Ge<sup>(32)</sup>, (×)  $\text{Bi}_2\text{Te}_3$  with Tl and Bi impurities as measured by this author, (□) off-stoichiometric  $\text{Bi}_2\text{Te}_3$ <sup>(24)</sup>. The data points represent this author's own measurements as well as a collection of literature data.

## Bismuth Tin Telluride

### Literature Review

$\text{Bi}_2\text{Te}_3$  can be doped p-type with extrinsic group IV atoms (Ge, Sn, Pb) or n-type with group VII atoms (I). The impurity concentration of the acceptors does not match one-to-one with the excess hole or electron concentration, with 1.4-1.7 holes introduced for one lead atom depending on the occupied lattice site, and 1.3-1.4 electrons per one iodine atom.<sup>(34)</sup> Further, it is observed that hole concentration of tin doped samples has a lesser dependence. Zhitinskaya<sup>(34)</sup> reports that from the range of tin impurities of  $(1.2-6) \times 10^{19} \text{ cm}^{-3}$ , the hole concentration only varies from  $(2-5) \times 10^{18} \text{ cm}^{-3}$ . This corresponds to a doping efficiency of 0.06 holes per tin atom. This is thought to occur because tin, due to its higher electronegativity, helps to prevent the construction of antisite defects. At low atomic concentrations ( $<0.2 \text{ at\%}$ ), tin atoms primarily occupy  $\text{Te}^{(2)}$  sites.<sup>(35)</sup> Between 0.2-1 at%, they begin to occupy the  $\text{Te}^{(1)}$  sites. It is here where they are believed to create resonance levels.<sup>(35)</sup> These tin atoms are neutral with respect to the lattice, but accept electrons<sup>(35)</sup> from higher lying valence states and have a total hole concentration of  $<10^{19} \text{ cm}^{-3}$ . The band of tin impurity states lies near the edge of the second band, with Ref (33) reporting that it is 15 meV below the top of the highest band at 2K. The band is calculated to be  $\sim 10 \text{ meV}$  wide<sup>(34)</sup> using degenerate statistics and the four transport coefficients (Seebeck, Hall, Nernst, and resistivity). Also notable is that the introduction of Sn helps to stabilize the Seebeck coefficient of single crystals of  $\text{Bi}_2\text{Te}_3$  grown by the Czochralski method.<sup>(36)</sup> Additionally, Kulbachinskii reports that Sn may form a resonant level in  $\text{Bi}_2\text{Te}_3$ .<sup>(33)(37)</sup> The compositions that he investigated are of the form  $\text{Bi}_{2-x}\text{Sn}_x\text{Te}_3$ , with  $x = 0.0025, 0.0075, 0.0125, 0.03$ . He proposes the layout of energy levels as

depicted in Figure 23 where the energy spacing as proposed by Refs. (29),(33),(36) has been inserted.

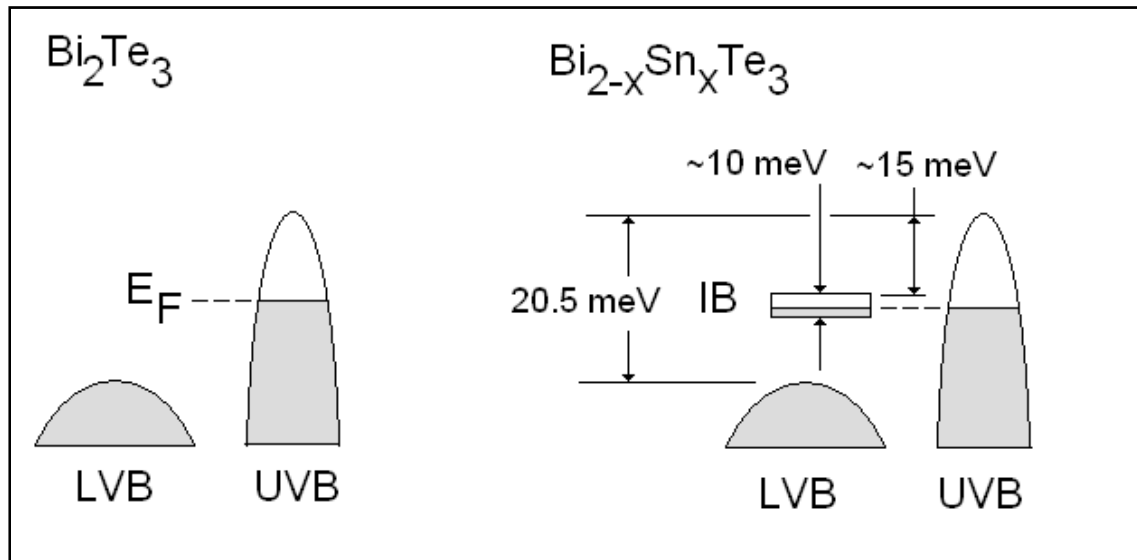


Figure 23: Schematic of valence band energy levels for  $\text{Bi}_2\text{Te}_3$  and  $\text{Bi}_{2-x}\text{Sn}_x\text{Te}_3$  from Ref. (33). The impurity tin state band is located 15 meV below the top of the upper valence band.

### Experimental

Bismuth telluride ( $\text{Bi}_{2-x}\text{Sn}_x\text{Te}_3$ ) with  $x=0.0025, 0.0075, 0.0150$  (corresponding to 0.05, 0.15, 0.30 at% Sn) single crystals were grown using a modified Bridgeman technique by V. A. Kulbachinskii at Moscow State University and tested at OSU. The samples' long axes were along the  $\langle 1 \rangle$  direction. Nernst, with  $B // \langle 3 \rangle$  direction, was measured from 77-400 K while Hall (also  $B // \langle 3 \rangle$ ) Seebeck, and resistivity were measured from 2-400 K. Shubnikov-de-Haas measurements were performed, with  $B // \langle 3 \rangle$  direction, at 1.9 K in order to determine the areas of the Fermi surfaces. Additionally, thermal conductivity measurements were made using the static heater and sink method; however, thermal radiative losses could not be accurately accounted for above room temperatures and only values up to 300 K are reported. From these measurements, we calculate and report  $zT$ ,

power factor, carrier density, Fermi level, mobility, effective mass, the Lorenz number, scattering parameter, electrical, lattice, and ambipolar thermal conductivities as functions of temperature.

### Shubnikov-de Haas

Shubnikov-de Haas (SdH) measurements were performed on the samples at 1.9K in magnetic fields up to 7 Tesla. Resistivity ( $\rho_{113}$ ) and Hall resistance ( $\rho_{123}$ ) were measured where the magnetic field was in the  $\langle 3 \rangle$  direction, current flux was in the  $\langle 1 \rangle$  direction, and the voltage in the  $\langle 1 \rangle$  direction for resistivity and  $\langle 2 \rangle$  direction for Hall resistance. Figure 24 shows oscillations in magnetoresistance. These are obtained after subtracting the polynomial background. At the highest tin concentration, the magnitude of the oscillations is greatly reduced over the other two samples; therefore, the error in the calculated magnetic field oscillation frequency will be greater. The oscillations observed as a function of B (Figure 24) are periodic when plotted as a function of  $1/B$ . A Fourier transform of this yields the harmonic content of the cyclotron frequency, at frequencies  $1/\Delta(1/B)$  in Tesla, and equation (3.45) gives the corresponding Fermi surface areas, as shown in Table 2.

Table 2. Tin concentrations and magnetic field oscillation frequencies and the corresponding Fermi surface areas for the three tested alloys. From Eq. (3.45)

Tin Content	Oscillation Frequency	Fermi Surface Area
$\text{Bi}_{2-x}\text{Sn}_x\text{Te}_3$	$[\Delta(1/B)]^{-1} \text{ T}$	$(\text{m}^{-2})$
$x=0.0025$	12.7	$1.21\text{E}+17$
	23.5	$2.24\text{E}+17$
$x=0.0075$	11.4	$1.09\text{E}+17$
	22.3	$2.13\text{E}+17$
$x=0.015$	13.5	$1.29\text{E}+17$
	22.1	$2.11\text{E}+17$

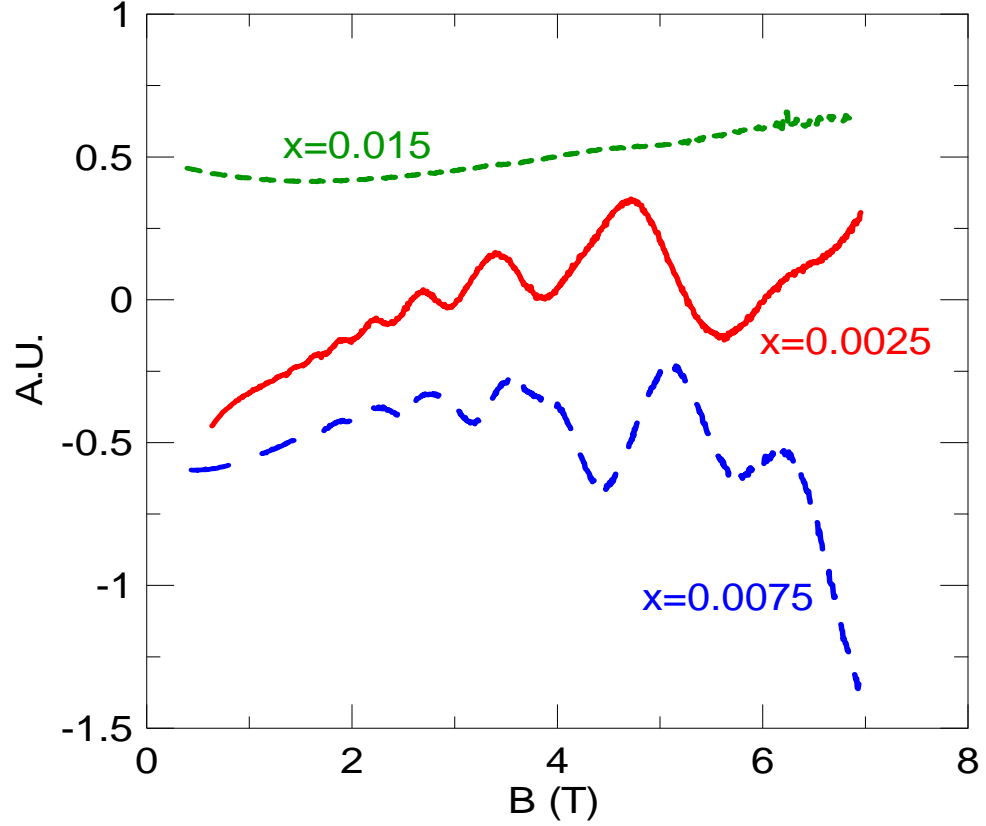


Figure 24: SdH oscillations for the three alloys. The curves have been shifted on the y-axis for ease of viewing. The symbols are: (solid line),  $\text{Bi}_{1.9975}\text{Sn}_{0.0025}\text{Te}_3$  (dashed line)  $(\text{Bi}_{1.9925}\text{Sn}_{0.0075}\text{Te}_3)$ , (dotted line)  $\text{Bi}_{1.985}\text{Sn}_{0.015}\text{Te}_3$ .

In order to analyze the Shubnikov-de Haas (SdH) data, we follow the methodology of Middendorff<sup>(38)</sup>, who demonstrated experimental evidence for a second valence band in  $\text{Bi}_2\text{Te}_3$ , which was greatly refined by Kohler<sup>(29)</sup>. We also include the results of Kulbachinskii for comparison. Above  $E_F = 20$  meV, Kohler reports that the 1<sup>st</sup> valence band becomes extremely non-parabolic. He further finds that the second valence band is located at  $E_F=20.5$  meV below the 1<sup>st</sup> band.

Looking at the samples tested here, we see that each sample has two oscillations, the higher of which is close to a second harmonic of the first. However, both Kohler and Middendorff also have samples that exhibit this behavior with oscillation frequencies that



are close to these two. Middendorff reports that the higher frequency surface corresponds to the upper valence band, which in turn has a larger Fermi surface. Following Ref (29), we find the cyclotron masses and use these to calculate the Fermi energy using the experimentally determined equation:

$$E_F(\text{in meV}) = \left[ \frac{\Delta m_c / m_e}{a(b + \Delta m_c / m_e)^{5/2}} \right]^{2/5}, \quad (6.1)$$

where  $a=2.97 \cdot 10^{-3}$  and  $b=m_c(0)/m_e=0.08$ ,  $m_e$  is the free electron mass,  $m_c$  is the cyclotron mass as found from SdH oscillations<sup>(29)</sup>,  $m_c(0)$  is the band edge cyclotron mass of the upper valence band (UVB in Figure 23), and  $\Delta m_c = m_c(E_F) - m_c(0)$ .<sup>(29)</sup>

Next, we calculate the effective mass density of states as the determinant of the mass tensor of the UVB using  $m_D^* = \alpha \cdot m_C^*$ , where  $\alpha=1.32$ .<sup>(29)</sup> We then calculate the carriers in the first band using the Fermi level and density of states effective mass (Eq. 3.14). If we plot our points onto Fig. 4 in Ref (38), we do not fall on the curves, this is because Middendorff did not take into account the change in cyclotron mass as the band fills. Subtracting the 2K Hall carrier density in the UVB derived this way leaves the number of carriers in the LVB band, and then we calculate their effective masses (Eq. 3.21). These results are presented in Table 3. Our measurements are in agreement with Fig. 9 in Ref. (29), which shows the Hall carrier density as a function of Fermi energy. This plot clearly demonstrates a large increase in Hall carrier density, which deviates from SdH carrier density, beginning at  $E_F=20.5$  meV. At the Fermi levels reached in these samples, the slope of Hall carrier density vs.  $E_F$  becomes very steep, which indicates that the LVB has

a very heavy mass. We see a decreasing carrier density in the 1<sup>st</sup> band and an increasing carrier density in the 2<sup>nd</sup> band with increasing tin concentration.

Conversely, we can also follow the methodology of Kulbachinskii, who regards the second oscillation in SdH as a resonance induced by Sn itself. We then calculate Fermi level using the cyclotron mass of the first Fermi surface and show these in Figure 25. In this Figure, we combine Kolher's data from Fig 9 in Ref. (29), Kulbachinskii's points from Ref. (37) and the present work. If we follow Kohler's method, we have the points represented by squares. These align well with the Fermi level and increasing carrier density in the LVB. Kulbachinskii's method yields the triangle data points. We see that one point falls close with his measurements; the others have significant deviation. From these measurements, we are unable to conclude which method is correct.

We note that the three samples here,  $x=0.0025$ ,  $0.0075$ ,  $0.015$ , have increased 260K thermopower of 15%, 40%, and 90% over that of the Pisarenko plot calculated using just the UVB. This leads to the main conclusion of this thesis. Both the Sn-induced resonant level and the LVB have heavy masses and both offer a major opportunity to considerably enhance the  $zT$  of  $\text{Bi}_2\text{Te}_3$ . Since it is likely that a heavier hole concentration is optimal, we can explore two avenues toward high- $zT$ : (1) heavy Sn doping; (2) double doping with both Sn and another acceptor such as Pb.

Table 3: Material parameters that have been calculated using the SdH measurements following the Kohler method.<sup>(30)</sup> Note that the density of states effective mass in the second band becomes increasingly large with increasing carriers in the second band. Refer to Figure 25.

Tin Content	Hall 2K carrier density	Cyclotron mass	Fermi Level	$m_D^*$ 1 <sup>st</sup> band	Carriers in 1 <sup>st</sup> band	Carriers in 2 <sup>nd</sup> band	$m_D^*$ 2 <sup>nd</sup> band
$\text{Bi}_{2-x}\text{Sn}_x\text{Te}_3$	$p \text{ (cm}^{-3}\text{)} \cdot 10^{18}$	$m_c^*/m_e$	meV	$m_D^*/m_e$	$p \text{ (cm}^{-3}\text{)} \cdot 10^{18}$	$p \text{ (cm}^{-3}\text{)} \cdot 10^{18}$	$m_D^*/m_e$
x=0.0025	2.78	0.118	23.44	0.156	.966	1.814	1.89
x=0.0075	4.44	0.115	23.26	0.152	.917	3.523	3.30
x=0.015	5.63	0.113	23.14	0.149	.882	4.748	4.19

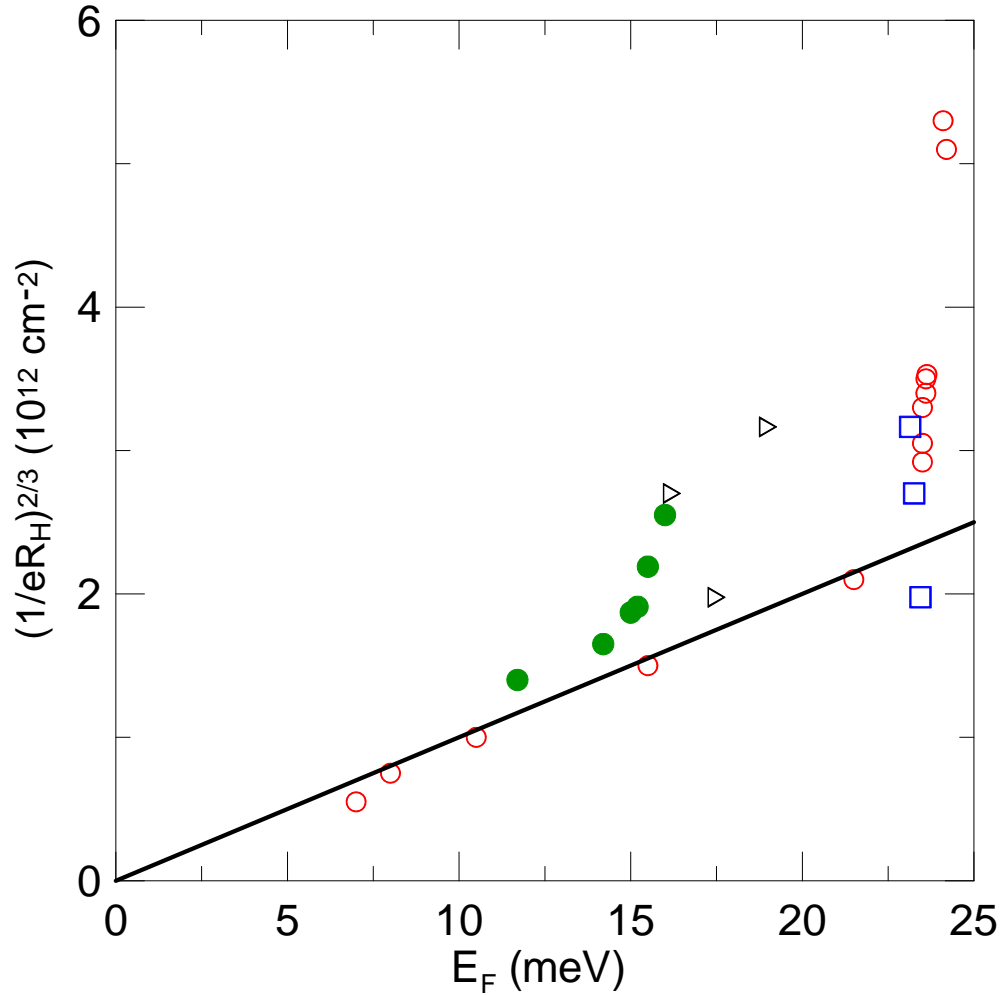


Figure 25: The symbols are (●)  $\text{Bi}_{2-x}\text{Sn}_x\text{Te}_3$  from (33), (○)  $\text{Bi}_2\text{Te}_3$  from (29), (□)  $\text{Bi}_{2-x}\text{Sn}_x\text{Te}_3$  from this work. The solid line is the calculated curve for  $\text{Bi}_2\text{Te}_3$  from (29). We note the deviation from the line at 15 meV for Kulbachinskii and 23 meV for Kohler.

## **Experimental Measurements and Interpretation of Transport Data at Low Magnetic Fields**

The materials next underwent galvanomagnetic and thermomagnetic measurements described in Section 2. A conventional flow cryostat was used in the range 80-400 K and -1.5 to 1.5 Tesla. Additionally, resistivity, Hall and Seebeck coefficients were measured at liquid helium temperatures. We use these measurements to calculate the transport properties of Fermi level, carrier mobility, carrier effective mass, and scattering parameter. Refer to Figure 26 where the results of the measurements are collected for the following discussion on the measured properties. There is a sharp peak in electrical resistivity for both  $x=0.0075$  and  $x=0.015$  at 60 K followed by a decrease and then slight increase with increasing temperature. The  $x=0.0025$  does not exhibit this peak, although it does contain inflection points in the resistivity trace at temperatures that correspond the same points in the higher doped samples. The Hall coefficient in all three samples varies little from 2-20K and then shows a sharp decrease over the temperature ranges 20-120K. It then stays approximately linear with a slight negative slope (indicating a higher doping concentration as the Fermi energy moves deeper in the valence band) until the onset of intrinsic conduction (both holes and thermally excited electrons) is witnessed and the Hall coefficient rapidly drops negative. In the temperature range studied, only the  $x=0.0025$  sample exhibits the onset of intrinsic conduction, which is reflective of its larger Hall coefficient and thus lower doping concentration. The samples show a smaller Hall coefficient with increasing tin concentration, which is expected since the samples are more metallic. The onset of intrinsic conduction is witnessed at a lower temperature in the Seebeck coefficient, which peaks and drops off at higher temperature for all

samples, with the  $x=0.0025$  peaking first and the  $x=0.015$  last. This Seebeck and Hall coefficients' behavior are consistent with each other. The Nernst coefficient is the largest for  $x=0.0025$  and changes from negative at low temperatures to positive at high temperature, with its zero point crossing at approximately the same temperature where the Seebeck peaks. This is a clear indication of balance in hole and electron density as described by Ref (1).

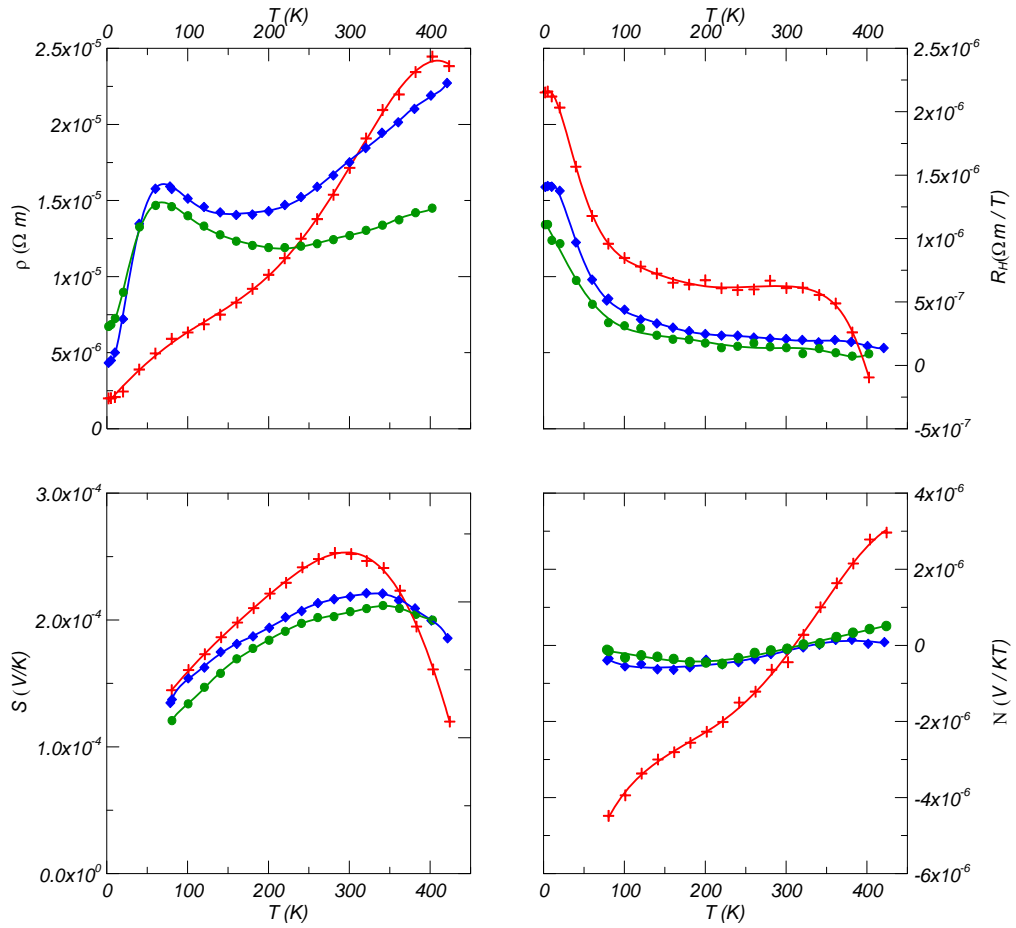


Figure 26: Galvanomagnetic (resistivity  $\rho$  and Hall coefficient  $R_H$ ) and thermomagnetic (Seebeck  $S$  and isothermal transverse Nernst ( $N$ ) coefficients) data as a function of temperature for the samples studied. The points indicate the measured data, while the lines are added to guide the eye. The symbols are: (+)  $\text{Bi}_{1.9975}\text{Sn}_{0.0025}\text{Te}_3$ , (◆)  $\text{Bi}_{1.9925}\text{Sn}_{0.0075}\text{Te}_3$ , (●)  $\text{Bi}_{1.985}\text{Sn}_{0.015}\text{Te}_3$ .

We plot in Figure 27 the power factor and hole carrier concentration. As hinted towards in the Seebeck and resistivity measurements, the power factor peak shifts towards higher temperature with higher tin content. Interestingly, the  $x=0.0075$  has the lowest peak power factor, of  $3.4 \text{ mW/mK}^2$  at  $260 \text{ K}$  and  $x=0.0025$  has the highest of  $4.8 \text{ mW/mK}^2$  at  $200 \text{ K}$ . There is an increase in the number of carriers with increasing temperature and tin concentration.

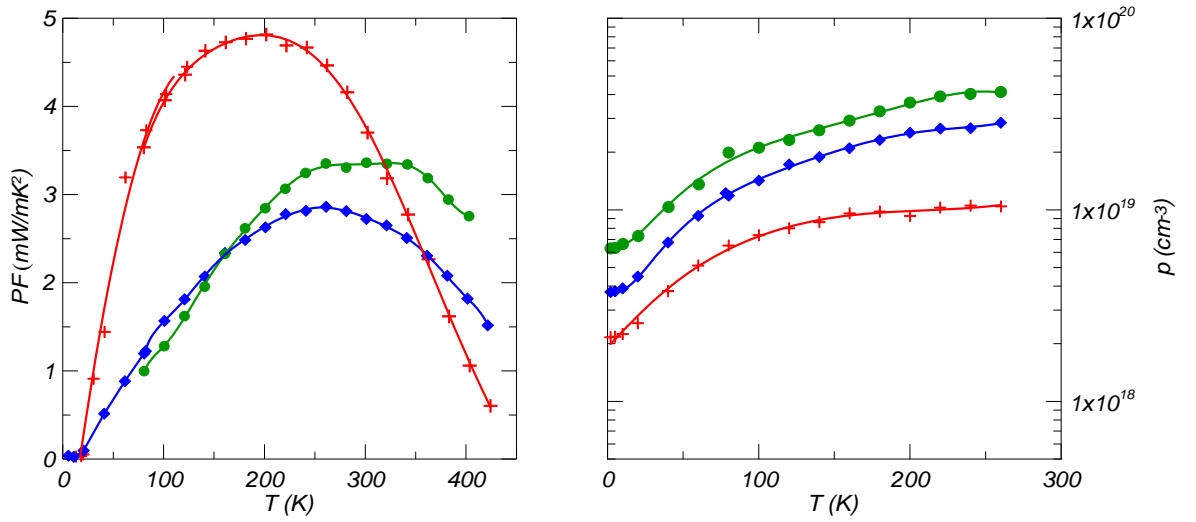


Figure 27: Power factor on the left and hole carrier densities for the alloys. Note the symbols are: (+)  $\text{Bi}_{1.9975}\text{Sn}_{0.0025}\text{Te}_3$ , (◆)  $\text{Bi}_{1.9925}\text{Sn}_{0.0075}\text{Te}_3$ , (●)  $\text{Bi}_{1.985}\text{Sn}_{0.015}\text{Te}_3$ .

The results of the four parameter fit are depicted in Figure 28. We note that the Fermi level of the samples trend downward toward the SdH calculated levels of 15~23 meV. While it appears that they may be heading lower, it is important to remember that the Hall coefficient and resistivity undergo a change due to the temperature dependence of the activation of tin. We note that the effective mass of the samples is increased over that of a reference  $\text{Bi}_2\text{Te}_3$  for the  $x=0.0075$ , 0.015 samples and approximately equal for  $x=0.0025$ . Electrical mobility drops with increasing hole concentration, which is to be

expected, and the presence of tin acts as an ionized impurity, thus leading to an increase in scattering.

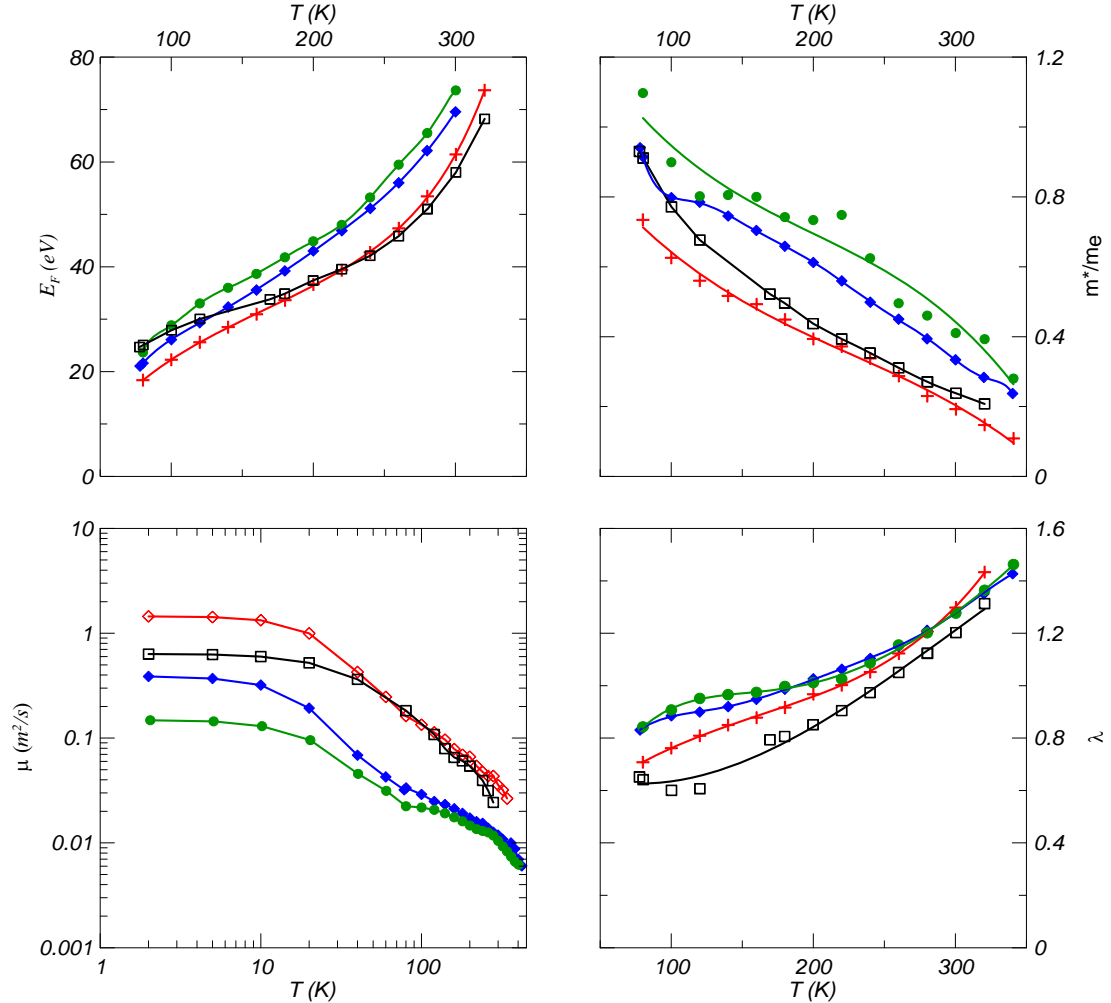


Figure 28 : Summary of four parameter fit using the degenerate equations. A pure  $\text{Bi}_2\text{Te}_3$  sample is included for reference; however, this sample has a higher doping level, which is reflected in a smaller mobility and higher Fermi level at low temperature. Note the symbols are: (+)  $\text{Bi}_{1.9975}\text{Sn}_{0.0025}\text{Te}_3$ , ( $\blacklozenge$ )  $\text{Bi}_{1.9925}\text{Sn}_{0.0075}\text{Te}_3$ , ( $\bullet$ )  $\text{Bi}_{1.985}\text{Sn}_{0.015}\text{Te}_3$ .

Figure 29 shows the total thermal conductivity of the samples and their figure of merit. Note that the increasing concentration of tin shifts the peak in  $zT$  to higher temperatures. The lack of a trend in thermal conductivity is also intriguing and may be due to an inaccuracy in the measurement. This may have occurred because of the differing

area/length ratio of the measured samples leads to varying radiative losses that create differing errors in the measurements. Following the methodology of Section 3, we calculate the Lorenz numbers. As shown in Figure 30, the samples have close Lorenz numbers, which are shown as a ratio to the free electron Lorenz number,  $L_0$ . Further, the electrical thermal conductivity of the samples is small, approximately 20% of the total thermal conductivity. The higher thermal conductivity of the  $x=0.0025$  sample can be partially explained by the presence of ambipolar thermal conductivity,<sup>(31)</sup> as discussed in Section 3. Using the calculated partial electron and hole Seebecks and conductivities, the ambipolar thermal conductivity for the  $x=0.0025$  material is calculated and shown in Figure 31.

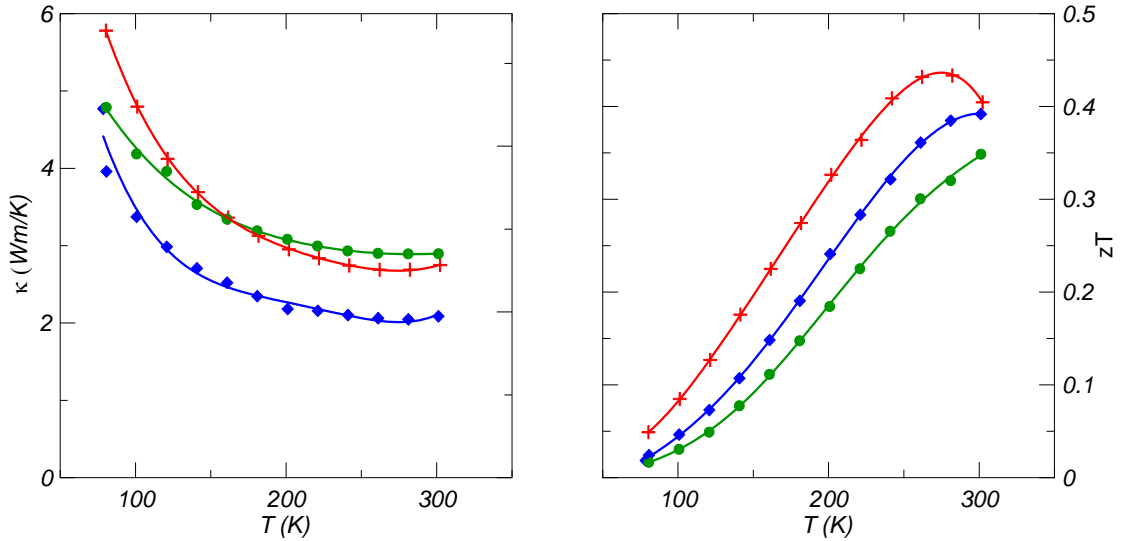


Figure 29: These plots show the total thermal conductivity and  $zT$  for the  $\text{Bi}_{2-x}\text{Sn}_x\text{Te}_3$  samples. Note that these samples have radiative heat loss errors that cannot be corrected. Increasing tin concentration shifts the peak  $zT$  to the right. Note the symbols are: (+)  $\text{Bi}_{1.9975}\text{Sn}_{0.0025}\text{Te}_3$ , (◆)  $\text{Bi}_{1.9925}\text{Sn}_{0.0075}\text{Te}_3$ , (●)  $\text{Bi}_{1.985}\text{Sn}_{0.015}\text{Te}_3$ .



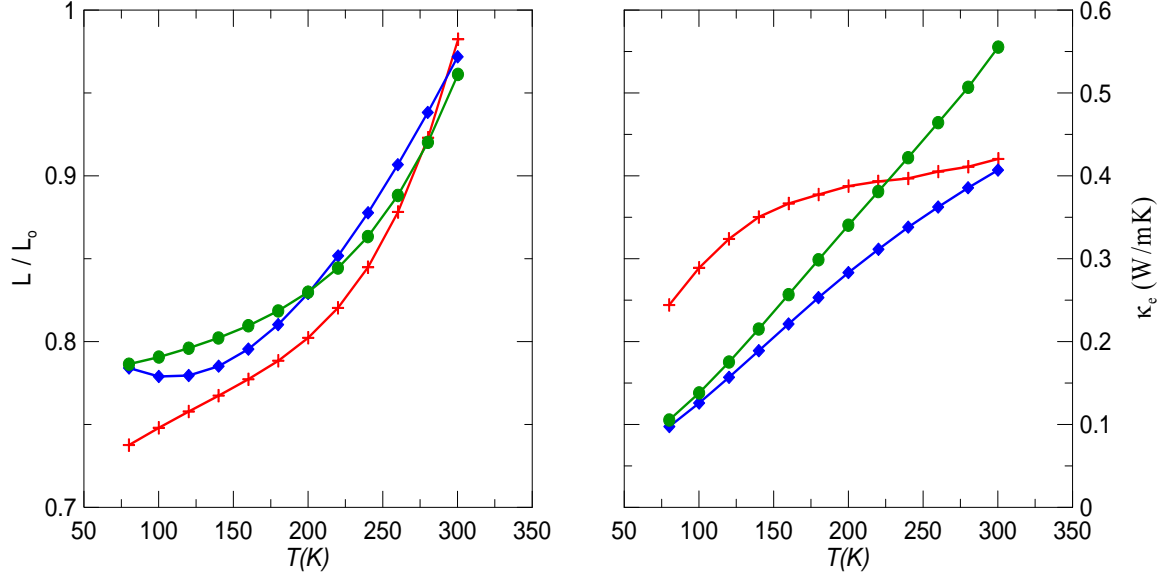


Figure 30: Lorenz number over free electron Lorenz number on the left and electronic thermal conductivity as calculated from the Lorenz number and electrical resistivity. Note the symbols are: (+)  $\text{Bi}_{1.9975}\text{Sn}_{0.0025}\text{Te}_3$ , ( $\blacklozenge$ )  $\text{Bi}_{1.9925}\text{Sn}_{0.0075}\text{Te}_3$ , ( $\bullet$ )  $\text{Bi}_{1.985}\text{Sn}_{0.015}\text{Te}_3$ .

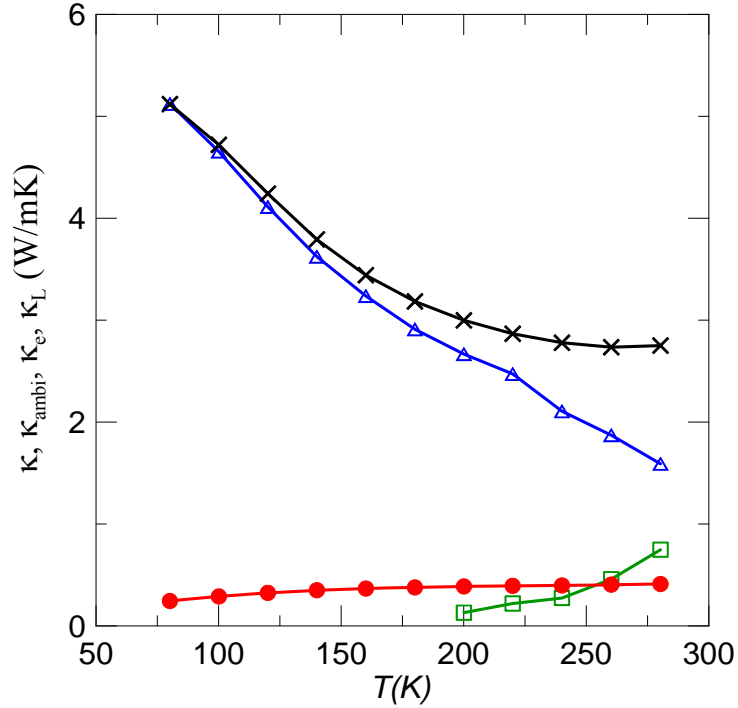


Figure 31: Total, lattice, electrical, and ambipolar thermal conductivity for  $\text{Bi}_{1.9975}\text{Sn}_{0.0025}\text{Te}_3$ . The symbols are: ( $\times$ ) total thermal conductivity, ( $\Delta$ ) lattice, ( $\bullet$ ) electronic, and ( $\square$ ) ambipolar.

### **Foundation for Increase in Thermopower in Bismuth Tin Telluride**

A deciding characteristic in the formation of a resonant level is the increase in Seebeck over that of a sample with the same carrier density, refer to Figure 22. Similarly, we notice in Figure 26 and Figure 32 a large enhancement in Seebeck over the  $T^1$  law we should have observed if we only had the UVB filled. Referring back to Mott's formula (1.22) we note that without a modification in the density of states, Seebeck should follow the straight  $T^1$  line shown in Figure 32 down to zero. We do see, in the temperatures below 10K, for  $x=0.0075$ , an increase in Seebeck which we attribute to phonon drag. Figure 32 contains the thermopower and carrier densities for the  $x=0.0025$ ,  $0.0075$  samples measured to liquid helium temperatures. Shown as the  $T^1$  trace is the solid line, which is what thermopower would follow if there are no modifications in the density of states, and  $m_D^*=0.15$  me (UVB only). Clearly, the  $\text{Bi}_2\text{Te}_3$  samples do not follow a  $T^1$  law and demonstrate a significant enhancement in Seebeck in the 15-50 Kelvin range. At higher temperatures, thermal smearing begins to affect the hole thermopower, and it becomes compensated.

We do want to note that the  $\text{Bi}_{1.95}\text{Sn}_{0.0025}\text{Te}_3$  sample had a Seebeck that was turning over at 300 K due to the onset of intrinsic conduction, where the strong decrease in  $S$  is now due to the appearance of thermally excited electrons. Therefore, we plot the Pisarenko curve at 260 K (instead of at 300K in Figure 22) and place the points to truly see where they lie before we hit the intrinsic regime. Figure 33 shows that the points do fall above the curve as calculated for  $\Lambda=3/2$ . From this, we further confirm that  $\text{Bi}_2\text{Te}_3$  alloyed with tin does increase the thermopower for a given carrier concentration.

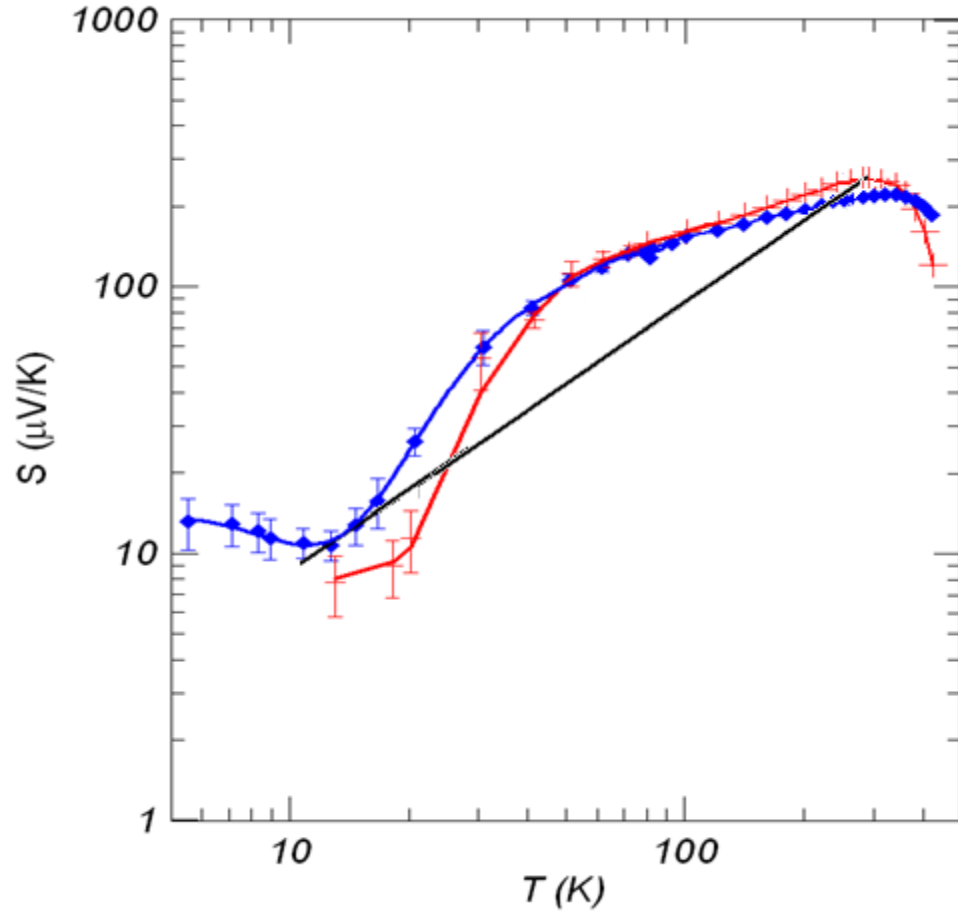


Figure 32: Plot of Seebeck for  $x=0.0025, 0.0075$  samples at lower temperatures on a log-log scale. The symbols are (+),  $\text{Bi}_{1.9975}\text{Sn}_{0.0025}\text{Te}_3$  (◆)  $\text{Bi}_{1.9925}\text{Sn}_{0.0075}\text{Te}_3$ , and the  $T^1$  trace to (0,0) from the peak Seebeck and corresponding temperature for  $\text{Bi}_{1.9975}\text{Sn}_{0.0025}\text{Te}_3$ . This trace is calculated for  $m_D^*$  from UVB and  $\lambda=3/2$ .

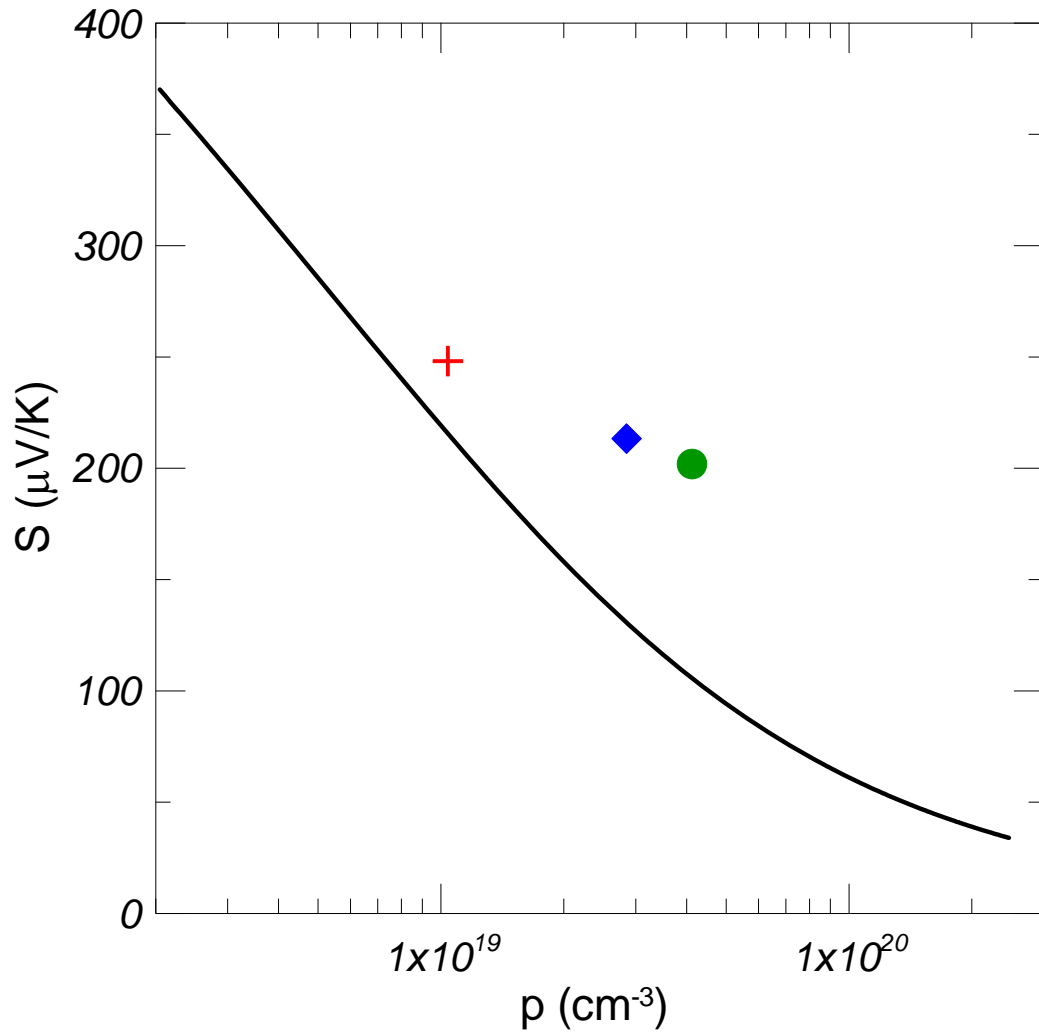


Figure 33: Pisarenko relation for  $\text{Bi}_2\text{Te}_3$  as calculated for 260 K. We note that these samples fall far above the line. Note the symbols are: (+)  $\text{Bi}_{1.9975}\text{Sn}_{0.0025}\text{Te}_3$ , (♦)  $\text{Bi}_{1.9925}\text{Sn}_{0.0075}\text{Te}_3$ , (●)  $\text{Bi}_{1.985}\text{Sn}_{0.015}\text{Te}_3$ .

## 6) CONCLUSION

In this thesis we characterize the galvanomagnetic and thermomagnetic properties of two promising thermoelectric material systems: PbSnTe-PbS and  $\text{Bi}_2\text{Te}_3\text{:Sn}$ . From these measured properties we were able to calculate basic properties that allow for a deeper understanding of why the materials have desirable thermoelectric traits. The PbSnTe-PbS system is effective because the nanoinclusions of PbS into the PbSnTe matrix increase the scattering coefficient and decrease the lattice thermal conductivity. Unfortunately, the decrease in effective mass counteracts the effect that the higher scattering coefficient has on Seebeck. The 8% PbS was found to be the highest  $zT$  sample, as it had a large enough reduction in electrical resistivity to counteract the decrease in thermopower effect that is attributed to modification of effective mass.

A Seebeck vs. carrier concentration relation was developed for  $\text{Bi}_2\text{Te}_3$  and used for comparison purposes.  $\text{Bi}_{2-x}\text{Sn}_x\text{Te}_3$  demonstrates an increase in thermopower for a given carrier concentration over that of pure  $\text{Bi}_2\text{Te}_3$ . In order to determine the underlying reason for this phenomena, Shubnikov-de Haas measurements were performed. Our analysis indicated that either a tin resonant state was created or the lower valence band was being filled with high mass carriers. Both in turn lead to an increase in Seebeck coefficient. We conclude from that part of the work that by doping  $\text{Bi}_2\text{Te}_3$  more heavily p-type than in the case of commercial TE alloys, one could reach the LVB and increase  $zT$  considerably.

## WORKS CITED

1. Putley, E. H. *Hall Effect & Related Phenomena*. London : Butterworth & Co. Limited, 1960.
2. Ravich, Y.I. *Semiconducting Lead Chalcogenides*. New York : Plenum Press, 1970.
3. Agrist, Stanley. *Direct Energy Conversion*. Allyn and Bacon, 1965.
4. Harman, T.C. and Honig, J. M. *Thermoelectric and Thermomagnetic Effects and Applications* Mc-Graw Hill, 1967.
5. *"Increased Thermoelectric System Thermodynamic Efficiency by Use of Convective Heat Transport*., Bell, L. Long Beach, CA : 21st International Conference on Thermoelectrics, 2002.
6. , *"Use of Thermal Isolation to Improve Thermoelectric System Operating Efficiency*., Bell, L. Long Beach, CA : Proceedings of the 21st International Conference on Thermoelectrics, 2002.
7. *Thermoelectric Properties of Complex Zintl Phase*. Snyder, G.J. American Physical Society, March 2008, New Orleans, LA.
8. *Thin-film thermoelectric devices with high room-temperature figures of merit -*. Venkatasubramanian, R. 597-602, Nature, 2001, Vol. 413.
9. *Cubic AgPbmSbTe<sub>2+m</sub>: Bulk Thermoelectric Materials with High Figure of Merit*. Hsu, K.F. Science, 2004, Vol. 303. 818
10. *Cooling, Heating, Generating Power, and Recovering Waste Heat with Thermoelectric Systems*. Bell, Lon E, Science, 2008, Vol. 321.
11. *Spinodal Decomposition and Nucleation and Growth as a Means to Bulk Nanostructured Thermoelectrics: Enhanced Performance in Pb<sub>1-x</sub>Sn<sub>x</sub>Te-PbS*. Androulakis, J. Am. Chem. Soc., 2007, Vol. 129. 9780-9788
12. *Enhancement of Thermoelectric Efficiency in PbTe by Distortion of the Electronic Density of States*. Heremans, J. P. Jovovic, V. Science, 2008, Vol. 321. 554
13. Girard, Steven. 2007. MRS Boston. p. Session 3.
14. *The best thermoelectric*. Mahan, G. Sofo, J., Proc. Natl. Acad. Sci. USA, 1996, Vol. 93.
15. *Thermoelectric Figure of merit of a one-dimensional conductor*. Hicks, L.D., Dresselhaus, M.S. Physical Review B, 1993, Vol. 47.

16. *Thermoelectric Power of Bismuth Nanocomposites*. Heremans, J.P. Physical Review Letters, 2002, Vol. 88.
17. *On the enhancement of the figure of merit in bulk nanocomposites*. Thiagarajan, S.J. Physica Status Solidi (a), Vol. 1.
18. *A New Phenomenon in the Change of Resistance in a Magnetic Field of Single Crystals of Bismuth*. de Haas, W. J. and Shubnikov, L. London : Nature, 1930, Vol. 126. 3179,
19. Ziman, J. M. *Electrons in Metals*. London : Taylor and Francis, LTD, 1962.
20. Khokhlov. *Lead Chalcogenides*. Taylor & Francis, 2002.
21. *Thermopower enhancement in PbTe with Pb precipitates*. Heremans. J. A. P., 98, 2005.
22. *A Contribution to the Phase Diagram of the Quasibinary System Pb[S<sub>(1-x)</sub>Te<sub>x</sub>]*. V., Leute. Z. Phys. Chem. (Muenchen), 1985.
23. A.F., Ioffe. *Physics of Semiconductors*. New York : Academic Press Inc., 1960.
24. Scherer, Scherer. Bismuth Telluride, Antimony Telluride, and their Solid Solutions. Rowe. *CRC Handbook on Thermoelectrics 1995*. 1995.
25. *de Haas-van Alphen Effect in n-Type Bi<sub>2</sub>Te<sub>3</sub>*. Mallinson, R.B., Rayne, J.A., Ure, R.W. , Phys. Rev., 1968, Vol. 175.
26. *Anisotropy of the Constant Energy Surfaces in Bi<sub>2</sub>Te<sub>3</sub> and Bi<sub>2</sub>Se<sub>3</sub> from Galvanomagnetic Coefficients*. Caywood, L.P., Miller, G.R.: Physical Review B, 1970, Vol. 2.
27. Sehr, R., Testardi, L. R., J. Phys. Chem. Solids, 1962, Vol. 23. 1219
28. *Non-Parabolicity of the Lowest Conduction Band in Bi<sub>2</sub>Te<sub>3</sub> from Shubnikov-de Haas Effect*. Kohler, H. Physica Status Solidi (b), 1976, Vol. 73.
29. *Non-parabolicity of the Highest Valence Band of Bi<sub>2</sub>Te<sub>3</sub> from Shubnikov-de Haas Effect*. Kohler, H. Physica Status Solidi (b), 1976, Vol. 74. 591
30. Shoemaker, G. E., Rayne, J. A., Ure Jr., R. W. Physical Review B, 1969, Vol. 185. 1046
31. *Electrical and Thermal Properties of Bi<sub>2</sub>Te<sub>3</sub>*. Satterthwaite, C.B., Ure. R.W. 5 Physical Review, 1957, Vol. 108 1164.
32. Bergmann. Z Natuforsch, 1963, Vol. 18a. 1169
33. *Thermoelectric Power and Scattering of Carriers in Bi<sub>2-x</sub>Sn<sub>x</sub>Te<sub>3</sub> with Layered Structure*. V.A., Kulbachinskii. Physical Status Solidi (b), 1997, Vol. 199. 505
34. Zhitinskaya, M.K. Fiz. Tverd. Tela, 40 8 1998.
35. Zhitinskaya, M.K. Fizika Tverdogo Tela, Vol 45, No. 7, 2003.

36. Zhitinskaya, M.K. Fizika i Tekhnika Poluprovodnikov, Vol 34 No 12, 2000.
37. *Valence-Band Energy Spectrum of Solid Solutions*. Kulbachinskii, V.A. Physical Review B, 1994, Vols. 50, 23, 16921.
38. *Evidence for a Second Valence Band in p-type  $\text{Bi}_2\text{Te}_3$  from Magneto-Seebeck and Shubnikov-de Haas Data*. Middendorff A. von, Landwehr, G. Solid State Communications, 1972, Vol. 11. 203
39. *Materials for Thermoelectric Energy Conversion*. Woods, C. Rep. Prog. Phys. 51 (1988) 459-539.